Quantifying geomorphological evolution from 10Be denudation rates: Insights from high-resolution depth profiles, topsoils, and stream sediments (Strengbach CZO, France)

Julien Ackerer, Jérôme van der Woerd, Anne Sophie Meriaux, Coralie Ranchoux, Gerhard Schäfer, Frederick Delay, François Chabaux

To cite this version:

Julien Ackerer, Jérôme van der Woerd, Anne Sophie Meriaux, Coralie Ranchoux, Gerhard Schäfer, et al.. Quantifying geomorphological evolution from 10Be denudation rates: Insights from high-resolution depth profiles, topsoils, and stream sediments (Strengbach CZO, France). Earth Surface Processes and Landforms, 2022, 10.1002/esp.5454 . insu-03762821

Quantifying geomorphological evolution from ^{10}Be denudation rates: insights from high-resolution depth profiles, topsoils and stream sediments (Strengbach CZO, France)

Ackerer J.[1,2*], Van der Woerd J.[1*], Meriaux A.S.[1], Ranchoux C.[1], Schäfer G.[1], Delay F.[1], Chabaux F.[1*]

[1]Institut Terre et Environnement de Strasbourg, UMR 7063 CNRS-Université de Strasbourg - ENGEES, 5 rue René Descartes, 67084 Strasbourg Cedex, France.

[2]Institut des Géosciences de l'Environnement, Université Grenoble Alpes, CNRS, 460 rue de la Piscine, 38400, Saint Martin d'Hères.

*corresponding authors: julien.ackerer@orange.fr; jerome.vanderwoerd@unistra.fr; fchabaux@unistra.fr

Keywords : ^{10}Be isotopes, geomorphological evolution, denudation rates, watershed.

Acknowledgments

This study was financially supported by the French ANR program under grant agreement ANR-15-CE06-0014 (Project CANTARE-Alsace) and by the 2020 IPGS-LHyGeS project call (CNRS-University of Strasbourg). The study also benefited from the funding of a post-doctoral salary to Julien Ackerer by the Labex G-eau-Thermie (University of Strasbourg). Amelie Aubert, René Boutin, Thierry Perone and Elise Kali are thanked for their help during chemical analysis performed at the Cortecs-Pacite plateforme at ITES and Martine Trautmann for the sample preparation (EOST). Daniel Viville and Eric Pelt are thanked for their involvement in the pit sampling campaigns in 2013 and 2017 and Simon Schalck and Marie Claire Pierret for the sampling campaigns of sediments soils and rocks in 2011. We also thank the ASTER Team (G. Aumaître, Régis Braucher, Vincent Godard, K. Keddadouche) for the AMS measurements, which were performed at the ASTER AMS French national facility (CEREGE, Aix- en-Provence), supported by the INSU-CNRS, the French Ministry of Research and Higher Education, IRD and CEA. We are grateful to Julien Charreau (CRPG, Nancy) for the discussions concerning the GIS Toolbox Basinga. This work also benefited from the support of the OZCAR research infrastructure. We are also grateful to two anonymous reviewers and to an anonymous associate editor and the editor-in-chief Stuart Lane for their constructive comments which helped to improve the manuscript.

Quantifying geomorphological evolution from ^{10}Be denudation rates: insights from high-resolution depth profiles, topsoils and stream sediments (Strengbach CZO, France)

Keywords : ^{10}Be isotopes, geomorphological evolution, denudation rates, watershed.

Abstract

A rare dataset of in-situ ^{10}Be from high-resolution depth profiles, soils, rock outcrops and stream sediments is combined with geochemical analysis and modeling of regolith evolution to understand the variability of denudation rates in a mountain watershed (Strengbach critical zone observatory). High-resolution depth profiles are key to detect the presence of mobile regolith and to highlight how it affects the critical zone evolution. The modeling of regolith evolution and ^{10}Be concentrations along depth profiles allow to estimate both the cosmic ray exposure age (19 kyr) and the mean denudation rate (22 mm.kyr^{-1}) of the regolith without any steady-state assumption on ^{10}Be concentrations. Comparison with maximum denudation rates inferred from topsoil samples collected from the surface of the depth profiles and calculated using the temporal steady-state assumption of ^{10}Be concentrations highlight an overestimation of denudation by a factor of two. Maximum spatially-averaged denudation rates determined from stream sediment samples also likely overestimate denudation rates by a factor of two. These biases are significant for investigating the geomorphological evolution and we propose a method to correct denudation rates using the inherited ^{10}Be concentrations and the cosmic ray exposure age deduced from the high-resolution depth profiles. A key result is also that a steady-state of ^{10}Be concentrations and a steady-state of regolith thickness are two different equilibrium states that do not necessarily coincide. The comparison between locally corrected and spatially-averaged denudation rates indicates that the watershed geomorphology is not in a topographic steady-state but is modulated by regressive fluvial erosion. Nonetheless, our study demonstrates that even in a watershed where the steady-state assumption of ^{10}Be concentrations is not verified, the spatial variations of in-situ ^{10}Be concentrations in sediments still carry qualitatively relevant information on the geomorphological evolution of landscapes.

1. Introduction

Denudation, which is defined as the sum of chemical weathering and physical erosion, is a key process for understanding the Earth’s surface evolution. Denudation exhumes fresh bedrock, exerts a strong control on landscape structure, and carries regolith particles from watershed slopes to rivers (Vanacker et al., 2007; Lupker et al., 2012; Schoonejans et al., 2016). Quantifying denudation rates is important for the understanding of regolith residence time (Foster et al., 2015), the sediment transport in rivers (Dongen et al., 2019), the evolution of mountain ranges (Meyer et al., 2010), or the coupling between chemical and physical processes in the critical zone (CZ; West, 2012; Larsen et al., 2014).

In-situ terrestrial cosmogenic ^{10}Be is a powerful tool to study the Earth’s surface evolution and to gather quantitative estimates on denudation rates (e.g. Dixon and Riebe, 2014). Many studies used in-situ ^{10}Be to estimate watershed-scale averaged denudation rates from stream or river sediments (e.g. Brown et al., 1995; Granger et al., 1996). This widely used approach is based on several important assumptions: (1) the denudation is uniform over time and ^{10}Be concentrations have reached a steady-state, reflecting a balance between ^{10}Be cosmogenic production and ^{10}Be loss by denudation and radioactive decay. (2) each eroding area contributes quartz to the mixed sediment sample in proportion to its erosion rate (valid with a single lithology). (3) if several lithologies are present, the contributing rock types contain similar grain size distributions. (4) quartz is not enriched during weathering or transport. (5) sediment storage is minimal in the watershed. And (6) the denudational time scale is smaller than the timescale for radioactive decay (Von Blanckenburg, 2005; Dunai, 2010).

In parallel to the watershed-scale averaged denudation rates, soil and regolith denudation rates were also locally determined from in-situ ^{10}Be in topsoil samples (e.g. Riebe et al., 2003; Meyer et al., 2010). However, calculations based on topsoil samples only provide estimates of the minimum exposure age under the assumption of a negligible denudation or estimates of the maximum denudation rate under the assumption of steady-state ^{10}Be concentrations (Braucher et al., 2009). Soil denudation rates are frequently converted into soil or regolith production rates assuming a steady-state of regolith thickness (regolith denudation at the soil level is balanced by the regolith production at depth; e.g. Heimsath et al., 1997).

One of the major issues is that the steady-state of denudation and in-situ ^{10}Be concentrations may not be verified for watersheds with a complex evolution including the transport of mobile regolith along slopes or complex exposure histories (assumption 1, Von Blanckenburg, 2005). Many studies taking place in mountain regions with potentially young surfaces and/or mobile regolith do not quantify the impact of this assumption (e.g. Riebe et al., 2003; Meyer et al., 2010), primarily because the analysis of in-situ ^{10}Be in superficial samples cannot independently determine both regolith exposure age and denudation rate (Norton et al., 2010). Another problem is the lack of a clear distinction between three different equilibrium states that do not necessary coincide in time: the steady-state of denudation and ^{10}Be concentrations, the steady-state of regolith thickness, and the steady-state of geomorphology and topography.

Sampling of in-situ ^{10}Be depth profiles raises a new research perspective (e.g. Schaller et al., 2004; 2018; Ackerer et al., 2016; Hidy et al., 2018). By gathering regolith and bedrock samples and by combining the contributions from neutrons and muons in modeling approaches, depth profiles opened the possibility of determining both exposure ages and denudation rates (Braucher et al., 2009). Depth profiles also provided new opportunities to investigate the thickness of mobile regolith, the mixing processes near the surface, or the polyphase evolution of weathering profiles (Ackerer et al., 2016; Schaller et al., 2018).

We supplement the data obtained by Ackerer et al. (2016) for a high-resolution depth profile located on the summit of a mountain watershed (the Strengbach watershed). Two new high-resolution depth profiles in addition with topsoils, rock outcrops and stream sediments were sampled across the Strengbach watershed to gather a wide database of mineralogical, geochemical and in-situ ^{10}Be analyses. This rare combination allows us to investigate: (a) how the mobile regolith is generated and how it affects the critical zone (CZ) evolution, (b) how the assumption of steady denudation and ^{10}Be concentrations impacts the denudation estimates, (c) how denudation rates vary temporally and spatially in a mountain watershed and (d) what are the timescales to reach steady-state for ^{10}Be concentrations, regolith thickness and geomorphology.

The Strengbach watershed is a particularly well suited location to investigate these points as it is a small mountain watershed (0.8 km^2) with a complex evolution and a first order stream (Ackerer et al., 2016). The bedrock is relatively homogeneous (Fichter et al., 1998) and alluvial terraces or major zones of sediment storage were not observed in the watershed (Cotel et al., 2016). Quartz enrichment during weathering is not an issue and the denudational time scale is clearly smaller than the timescale for radioactive decay (Ackerer et al., 2016). By consequence, most of the assumptions classically used to interpret ^{10}Be data are validated in this mountain watershed (assumptions 2 to 6; Von Blanckenburg, 2005), with the exception of the critical assumption of balance between the productions and losses of ^{10}Be within the watershed (assumption 1). Our study will thus allow to focus on the specific impact of this major assumption on denudation estimates in a complex watershed.

2. Study site

This study was conducted in the Strengbach watershed (figure 1), one of the reference sites of the French critical zone network (OZCAR), where multidisciplinary studies have been conducted since 1986 (“Observatoire Hydrogéochimique de l’Environnement”, OHGE; Fichter et al., 1998; Viville et al., 2012; Ackerer et al., 2016; 2020a; Chabaux et al., 2017; 2019; Pierret et al., 2018; Wild et al., 2019; Ranchoux et al., 2021). The Strengbach watershed is a headwater watershed (0.8 km²) located in the Vosges Mountains of northeastern France at elevations between 883 and 1147 m (figures 1a and 1b).

The current climate is mountainous oceanic, with an annual mean temperature of 7 ˚C and an annual mean rainfall of approximately 1400 mm. An updated summary of the Strengbach hydrologic and climatic features can be found in Pierret et al. (2018). The bedrock is a Hercynian granite, fractured, hydrothermally overprinted, and mainly composed of quartz (35%), albite (31%), K-feldspar (22%) and biotite (6%). The granite was affected by weathering processes during the Quaternary (Ackerer et al., 2016) and the watershed is currently covered by a 50 to 100 cm-thick soil overlying a 0.5 to 8 m-thick regolith (Weill et al., 2019; Ackerer et al., 2020a). The regolith is defined here by the layer of weathered material that has lost a physical coherence with the bedrock in place. The granitic bedrock is outcropping at few locations, with tors located on the summit of the northern slopes and at mid-elevation on the southern slopes (figure 1).

The watershed geomorphology was likely affected by periglacial processes during the Quaternary as the Vosges massif experienced Pleistocene glaciations (Mercier et al., 1999;

Heyman et al., 2013). Cold conditions likely persisted at the elevation of the Strengbach watershed after the Late Glacial Maximum (LGM), and the forest cover probably developed only at the beginning of the Holocene (Leroy et al., 2000). The Strengbach watershed was affected by anthropogenic deforestation associated with pastoralism before the 20th century (Etienne et al., 2013), and the return to a dense forest is due to the planting of spruce stands at the beginning of the 20th century (Fichter et al., 1998).

3. Methods

3.1 Sampling methods

Samples were collected at different locations to explore the variability of denudation rates within the watershed (figure 1b). Two new high-resolution depth profiles extending from the topsoil (0 m) to the granitic bedrock (2-3 m) were realized by digging pits in the slope below the depth profile located on the summit and analyzed by Ackerer et al. (2016). These new depth profiles are located on a gentle slope of the southern part of the watershed where no modern perturbations are visible (figure 1b). Our high-resolution sampling includes: (1) a high number of samples (10 to 15), (2) a detailed density of sampling (one measure every 15-25 cm maximum) to identify specific zones along the vertical direction and (3) a sampling not neglecting the lower part of the depth profiles (the lower regolith and the bedrock), as this part contains important information for the long term muonic exposure and the inherited ^{10}Be. The three depth profiles are named P1, P2 and P3 (figures 1b and 1c). Observations were performed to study the CZ structure and to estimate soil and regolith thicknesses in the three profiles.

In addition, topsoil samples were collected at different places in the watershed, with independent topsoil samples taken on the top of depth profiles, and other samples taken at lower elevations and on the summit of the northern part of the watershed (figure 1b). Two rock samples were also collected on granitic tors outcropping nearby the summit of northern slopes and at mid elevation location on southern slopes (figure 1b). Stream sediment samples were finally collected along the Strengbach stream network before and at the watershed outlet (figure 1b).

3.2 Analytical methods

For samples collected in depth profiles, depth, major element concentrations, mineralogy, density and in-situ ^{10}Be concentrations were characterized (table 1, supplementary tables S1 and S2). For topsoil, rock outcrop and stream sediment samples, only density and in-situ ^{10}Be concentrations were characterized (table 2).

Bulk densities of regolith samples collected from depth profiles were estimated by combining measurements of fine fraction and block densities (Ackerer et al., 2016). For each sample in the upper part of profiles (0-100 cm), the fine fraction density was obtained by weighing a known volume of regolith sampled with a steel cylinder. The proportion of blocks was estimated via macroscopic description and photos and a constant density of 2.7 g.cm^{-3} was used for the granitic bedrock. The bulk density of each sample was then calculated by combining the fine fraction density and the density of blocks with respect to the proportion of blocks in the horizon.

Quartering and sequential crushing provided representative subsamples of regolith bulk samples. These subsamples were used for mineralogical, major elements, and in-situ ^{10}Be analysis following the methodology detailed in Ackerer et al. (2016). Mineralogical analysis was performed by X-ray diffraction, and major element concentrations were determined by tetraborate alkaline fusion followed by ICP-MS and ICP-AES analysis at ITES laboratory

(Institut Terre et Environnement de Strasbourg, France; Gangloff et al., 2014; Prunier et al., 2015) and BRGM (Bureau des Recherches Géologiques et Minières, Orléans, France). The analytical accuracy was checked by measuring the San Joaquin soil standard (NIST SRM 2709a), and the overall uncertainty was <5 % for major element concentrations.

For in-situ ^{10}Be, subsamples consist of approximately 150 g of 250-500 µm sieved grains. Purified quartz was obtained from regolith samples by following the approach involving sequential HCl and HF leaching to remove oxides, organic matter and meteoric beryllium (e.g. Kohl and Nishiizumi, 1992). After addition of a ^{9}Be carrier, beryllium separation, purification, hydroxylation, and targeting, the ^{10}Be/^{9}Be ratios were measured by accelerator mass spectrometry at ASTER (CEREGE laboratory, France). The ^{10}Be/^{9}Be ratios of the blanks and samples were approximately 1×10^{-15} and 1×10^{-13}, respectively, and the overall analytical uncertainty for ^{10}Be concentrations was <5 % (table 1).

3.3 Quantification of chemical mobility and volumetric variations in depth profiles

To quantify the mobility of major elements within each depth profile, mass transfer coefficients (τ_i) were calculated as (Brimhall et al., 1991; Riebe et al., 2003):

$$\tau_i = \left(\frac{C(i)_{sample}\,C(j)_{bedrock}}{C(i)_{bedrock}\,C(j)_{sample}} - 1\right) \quad (1)$$

with $C(i)_{sample}$ and $C(i)_{bedrock}$ the concentrations of the element i for a given sample and for the deepest sample of the depth profile, and $C(j)_{sample}$ and $C(j)_{bedrock}$ the concentrations of the immobile element j for a given sample and for the deepest sample of the depth profile. Positive or negative τ_i imply the gain or loss of the element i relative to the deepest bedrock sample of a profile, taken as the reference rock. Titanium (Ti) was used as an immobile element for the τ_i calculation due to evidence of immobile behavior during weathering in the profile P1 (Ackerer et al., 2016). In addition, volumetric strain index (ε) was calculated to quantify the volumetric variations within each depth profile as (Brimhall et al., 1991):

$$\varepsilon = \left(\frac{C(j)_{bedrock}\ \rho_{bedrock}}{C(j)_{sample}\ \rho_{sample}} \right) - 1 \quad (2)$$

with ρ_{sample} and $\rho_{bedrock}$ the bulk density values for a given sample and for the deepest sample of each depth profile, respectively. ε values close to zero indicate isovolumetric weathering, while positive or negative values indicate expansion or compaction.

4. Analytical results

4.1 Subdivision of depth profiles

Soil thickness is variable and reaches 50 cm, 70 cm and 80 cm in depth profiles P1, P2 and P3, respectively (table 1). Soil type changes from alocrisol in P1 to ochric podzol in P2 and P3, and few weakly weathered blocks of granite are observed within the upper soil in P2 and P3 (figure 1c). Lower regolith extends between 50 and 100 cm, 70 and 190 cm, and 80 and 190 cm of depth for P1, P2 and P3, respectively (table 1, figure 1). In P1, the amount of blocks gradually increases from top to bottom of the lower regolith, while the proportion of granitic grus decreases (figure 1c). In P2 and P3, the thicker lower regolith has a different texture, with higher amount of clay minerals and some large blocks showing angular and sharp faces with signs of transport. The amount of blocks is also much more variable along the vertical direction in P2 and P3. Granitic bedrock extends below 100 cm for P1 and below 190 cm for P2 and P3, respectively (figure 1c). Bedrock is in place for the three depth profiles and shows weaker traces of weathering. As also detailed in Ackerer et al. (2016), profile P1 has a simple and continuous vertical structure indicating a soil and a regolith developed from in-situ bedrock weathering. P2 and P3 show more complex vertical structures indicative of regolith mobility along the slope.

4.2 Mineralogy, chemical mobility and density in depth profiles

A clear enrichment of interstratified clay minerals is observed in the soil of all depth profiles (supplementary table S1). Minerals resistant to weathering tend to accumulate in the soil (quartz, K-feldspar) while illites, biotite and albite are depleted. Variations from bedrock to regolith are relatively smooth in profile P1 with enrichment of quartz and depletion of most other primary minerals (table S1). In P2 and P3, abrupt depletion of albite and enrichment of illites and micas occur at the transition between bedrock and mobile regolith. Albite is less depleted in the upper part of the mobile regolith (table S1), indicating a non-continuous weathering along the vertical direction in profiles P2 and P3.

τ_i values close to zero indicate limited mobility of major elements in the bedrock of the three profiles (figure 2, concentrations in table S2). In P1, τ_i values point to a progressive depletion of major elements from the bottom of the regolith ($\tau_{CaO} = -0.1$) to the topsoil ($\tau_{CaO} = -0.5$, figure 2a). In P2 and P3, the mobile regolith shows stronger variations of τ_i coefficients with marked depletion of sodium and calcium ($\tau_{Na2O} = -0.8$, 130 cm depth, P2, figure 2b; $\tau_{Na2O} = -0.7$, 180 cm depth, P3, figure 2c). τ_i values are less negative in the upper part of the mobile regolith and more negative in the soil of P2 and P3, supporting a non-continuous weathering along the vertical direction in these two profiles (figures 2b and 2c). These complex variations are less visible for silica, aluminum and potassium as these elements are controlled by less weatherable minerals (quartz, K-feldspar, …). Overall, the mobility of major elements follows the structure of depth profiles, with a progressive depletion of major elements in P1 and more complex variations in the mobile regolith of P2 and P3.

Bulk density is assumed constant in the bedrock of the three profiles (d=2.7 g.cm^{-3}) before decreasing in the lower regolith (d=1.8-2.6 g.cm^{-3}) and in the soil (d=0.9-1.8 g.cm^{-3}, table 1 and figure 3). Bulk density primarily follows the soil and regolith thicknesses. Volumetric variations are limited in the bedrock and the lower regolith, but expansion occurs in the soil of the three depth profiles (ε=0.5-1.4, figure 3b).

4.3 In-situ ^{10}Be variations in depth profiles

At first order, in-situ ^{10}Be concentrations increase towards the soil surface within the three depth profiles (table 1, figure 3a). ^{10}Be concentrations are similar in the granitic bedrock for all profiles with concentrations around 25000-30000 atoms. g qtz^{-1}. The exponential increase of ^{10}Be concentrations is continuous within the bedrock and the lower regolith of P1, while ^{10}Be concentrations show a linear trend in the soil of P1 (figure 3a). For P2 and P3 profiles, ^{10}Be concentrations show an exponential trend within the mobile regolith, but concentrations are systematically higher than the concentrations measured in the lower regolith of P1. ^{10}Be concentrations are also higher in the soil of P2 and P3 compared to P1, with scattered concentrations in the soil of P3 (figure 3a). Similarly to the profile subdivision and major elements, ^{10}Be concentrations point to a relatively continuous evolution in P1 and more complex variations in P2 and P3. This complexity tends to increase from the summit to the lower part of the hillslope.

4.4 In-situ ^{10}Be variations in topsoils, rock outcrops and stream sediments

In-situ ^{10}Be concentrations measured in topsoil samples tend to decrease with increasing elevation, with concentrations around 180000-190000 atoms. g qtz^{-1} near the main crests and concentrations around 200000-220000 atoms. g qtz^{-1} at mid-slope (table 2). ^{10}Be concentrations in rock outcrops are the highest measured in the Strengbach watershed with values of approximately 220000-230000 atoms. g qtz^{-1} (table 2). For the stream sediment samples, ^{10}Be concentrations are comparable in the upper part of the stream (around 190000 atoms. g qtz^{-1}, table 2). The stream sediment sample collected at the watershed outlet stands out with the lowest ^{10}Be concentration measured in surface samples across the watershed (table 2).

5. Modeling methods

Mean denudation rate and cosmogenic exposure age of profile P1 were determined from a numerical inverse procedure in Ackerer et al. (2016). Due to the complex structure of the two new depth profiles P2 and P3, an accurate estimation of denudation rates and exposure ages is not possible from a numerical inverse procedure for these profiles. We therefore propose a direct modeling of the evolution of the depth profiles P2 and P3 integrating regolith production, denudation, and the effect of the regolith mobility on ^{10}Be concentrations. This direct modeling of regolith evolution at the depth profile scale is supplemented by denudation rates derived from topsoil, rock outcrop and stream sediment samples.

Our modeling approaches are based on the same general differential equation describing the evolution of ^{10}Be concentration (C) as a function of depth and time (e.g. Lal, 1991):

$$\frac{\partial C}{\partial t} = P \ \exp\left(\frac{-\rho z}{K}\right) + d \ \frac{\partial C}{\partial z} - \lambda C \quad (3)$$

with P the total surface production rate (in atoms. g qtz^{-1}. yr^{-1}), t the cosmic ray exposure age of the profile (in yr), z the depth (in cm), ρ the integrated density (in g. cm^{-3}), K the attenuation length of cosmic ray particles (g. cm^{-2}), d the mean denudation rate of the surface (in cm. yr^{-1}) and λ the radioactive decay constant of the ^{10}Be (in yr^{-1}). This general differential equation 3 was adapted for the interpretation of ^{10}Be concentrations from depth profile, topsoil, rock outcrop and stream sediment samples.

5.1 Modeling of ^{10}Be concentrations in depth profiles

By considering constant values over time of inherited concentration from previous exposure C_0 and of respective proportions of secondary neutrons, negative muons and fast muons in ^{10}Be production, the evolution of ^{10}Be concentration (C) as a function of time (t), depth (z) and integrated density (ρ) for a given denudation rate (d) along a depth profile can be determined from equation 3 as (adapted from Siame et al., 2004):

$$
\begin{aligned}
C(t,z,\rho) = {} & C_0 \exp(-\lambda t) + \frac{P.P_n}{\frac{\rho d}{K_n}+\lambda} \exp\left(\frac{-\rho z}{K_n}\right)\left(1-\exp\left(-t(\frac{\rho d}{K_n}+\lambda)\right)\right) \\
& + \frac{P.P_{nm}}{\frac{\rho d}{K_{nm}}+\lambda} \exp\left(\frac{-\rho z}{K_{nm}}\right)\left(1-\exp\left(-t(\frac{\rho d}{K_{nm}}+\lambda)\right)\right) \\
& + \frac{P.P_{fm}}{\frac{\rho d}{K_{fm}}+\lambda} \exp\left(\frac{-\rho z}{K_{fm}}\right)\left(1-\exp\left(-t(\frac{\rho d}{K_{fm}}+\lambda)\right)\right) \qquad (4)
\end{aligned}
$$

with P_n, P_{nm} and P_{fm} the relative contributions of 97.85, 1.5 and 0.65 % to the total production rate P, and K_n, K_{nm} and K_{fm} the effective attenuation lengths of 150, 1500 and 5300 g.cm^{-2}, for secondary neutrons, negative muons and fast muons, respectively (Braucher et al., 2009).

- Modeling of depth profiles

A direct modeling was developed to determine the variations of soil and regolith production rates, soil and regolith thicknesses, and bulk and integrated densities during depth profile evolution (flow chart in supplementary figure S1). Simulations based on a finite difference scheme were performed for each depth profile along a 1D vertical direction. The CZ vertical structure was subdivided into three parts: the soil, the lower regolith and the bedrock. During simulations, a constant mean denudation rate d was imposed at the soil surface of each profile by following:

$$dz_{soil\_surface} = d * dt \quad (5)$$

with $z_{soil\_surface}$ the elevation of the soil surface. In parallel, the soil is formed from lower regolith weathering and the lower regolith is formed from bedrock weathering. Calculation of soil and regolith production rates was based on a law of exponential decline with increasing soil and regolith thicknesses (e.g. Heimsath et al., 2010; Ma et al., 2010):

$$F_{sol} = F_0 \ \exp(-\alpha \ h_{sol}) \quad (6)$$

$$F_{reg} = F_0 \ \exp(-\beta \ h_{reg}) \quad (7)$$

with h_{sol} and h_{reg} the soil and regolith thicknesses (in cm), F_{sol} and F_{reg} the production rates of soil and regolith (in g.cm^{-2}.yr^{-1}), F_0 the maximum soil and regolith production rate when soil and regolith thicknesses equal zero (in g.cm^{-2}.yr^{-1}), and α and β the depth scaling factors of soil and regolith production rates (in cm^{-1}). h_{sol} and h_{reg} were actualized at each new time step during simulations by considering the competition between soil surface lowering due to denudation and soil and regolith production. For the parameter F_0 governing the maximum soil and regolith production rate, we used for all profiles a high production rate determined by Egli et al. (2014) on a very thin regolith from a mountain environment (table S3). Scaling factors α and β controlling the exponential decrease of soil and regolith production rates with soil and regolith thicknesses were adjusted for each profile to obtain the best agreement between modeled and observed thicknesses at present time.

We assumed that bulk densities of topsoil, soil base and granitic bedrock remained constant through time and we used present day measurements of density for these three interfaces (values in table S3). Bulk density variations throughout the regolith were calculated by a linear interpolation between topsoil, soil base and bedrock densities. The integrated density at a given depth was then calculated by taking the average of bulk densities along the regolith column above the given depth.

- Initial state and inherited ^{10}Be

Previous modeling of ^{10}Be concentrations in the depth profile P1 located at the summit of the watershed indicated that a major erosion event removing the soil and part of the regolith occurred at approximately 19 kyr BP (Ackerer et al., 2016). This major erosion event removed approximately 2 m of material and was followed by a much more stable exposure period during the Holocene. The inherited ^{10}Be concentrations are derived from the deeper bedrock samples (≈15 000 atoms. g qtz^{-1}), that would correspond to a long-term muonic component equivalent to an exposure age of approximately 150 kyr.

Based on the results of Ackerer et al. (2016), a relic regolith in place and a bedrock in place were taken as initial state for the direct modeling of P1 at 19 kyr BP (parameters in table S3). Given the proximity of the three profiles, P2 and P3 were also probably affected by the major erosion event at 19 kyr BP. In addition, a mobile regolith within profiles P2 and P3 was highlighted by profile section descriptions and geochemical data (section 4). We therefore used an extremely thin soil after erosion, a mobile regolith stabilized on the slopes, and a bedrock in place as initial state for P2 and P3 at 19 kyr BP (table S3).

The inherited ^{10}Be concentration from previous exposure (C_0 in equation 4) was adapted for each depth profile in agreement with their initial states. In the bedrock of all depth profiles, C_0 was set to have an inherited ^{10}Be concentrations from a long-term muonic pre-exposure of 150 kyr (table S3). The same C_0 was used for the lower regolith of the profile P1, as the relic regolith probably experienced the same muonic exposure. By contrast, in the mobile regolith of P2 and P3, C_0 values represent the ^{10}Be concentrations in the regolith transported along the slope and stabilized on P2 and P3 after the important erosive event. C_0 values in the mobile regolith of P2 and P3 are unknown and were adjusted to obtain the best agreement between modeled and measured ^{10}Be concentrations in these profiles.

- Final ^{10}Be concentrations

The surface total ^{10}Be production rates were determined for the three depth profiles following Martin et al. (2017) (scaling LAL-ERA Musch). After this step, ^{10}Be production rates along depth were calculated for each time step from equation 4 and from the time evolution of the integrated density. Final ^{10}Be concentrations were computed by taking the sum of ^{10}Be produced during simulation time, and exposure age and denudation rate can be estimated by comparing modeled and observed ^{10}Be concentrations. Best fits were identified with the help of Kling-Gupta coefficients (Gupta et al., 2009). Overall, the denudation rate d is inferred from equation 4 with the help of the direct modeling of depth profile evolution that does not rely on a steady-state assumption for the ^{10}Be concentrations.

5.2 Modeling denudation rates from topsoil, rock outcrop and stream sediment samples

In-situ ^{10}Be concentrations are also widely used to estimate local or catchment-wide denudation rates from their analysis in topsoil, rock outcrop or stream sediment samples (e.g. Granger et al., 1996; Meyer et al., 2010; Portenga and Bierman, 2011). By assuming that there is no inherited ^{10}Be concentration, that ^{10}Be concentration has reached a steady-state, and that the exposure age is much longer than the effective irradiation time ($t \gg T_{eff}$; with $T_{eff} = \frac{1}{\lambda + \frac{\rho}{K_n} . d_{max}}$; Lal, 1991), the ^{10}Be concentration for a surface sample (z=0) can be expressed as (Charreau et al., 2019):

$$C(z_0) = \frac{P.P_n}{\frac{\rho.d_{max}}{K_n} + \lambda} + \frac{P.P_{nm}}{\frac{\rho.d_{max}}{K_{nm}} + \lambda} + \frac{P.P_{fm}}{\frac{\rho.d_{max}}{K_{fm}} + \lambda} \qquad (8)$$

with d_{max} the maximum denudation rate inferred from the surface sample. A good knowledge of spatial variations of ^{10}Be production rates is necessary for the calculation of d_{max} and for the comparison of its value inferred from samples collected at different locations. The d_{max} estimates were calculated similarly to Mariotti et al. (2019) using the GIS toolbox Basinga developed by Charreau et al. (2019), where d_{max} is approximated by:

$$d_{max} \approx \left(\frac{P.P_n}{C}\right)\frac{K_n}{\rho} + \left(\frac{P.P_{nm}}{C}\right)\frac{K_{nm}}{\rho} + \left(\frac{P.P_{fm}}{C}\right)\frac{K_{fm}}{\rho} \qquad (9)$$

We used a 5 m resolution digital elevation model (DEM) of the Strengbach watershed from the French National Geographic Institute (IGN, RGE ALTI® version 2.0) combined with the QGIS software to determine the geomorphological features (elevation, slope, area, …) across the watershed. Secondary neutrons, negative and fast muons were considered and we used the Lal/Stone time-dependent scaling model (Lal, 1991; Stone, 2000) and revised ^{10}Be production rates (Martin et al., 2017). Shielding effect is limited in the watershed and was estimated by following the method from Codilean (2006).

For topsoil and rock outcrop samples, local ^{10}Be production rates were calculated at each location and equation 9 gives the maximum denudation rate at the sample location (referred as local d_{max}). The local d_{max} obtained from a single topsoil sample independently collected on the surface of a depth profile can then be compared to the denudation rate d inferred from equation 4 to quantify the impact of the assumption of steady-state ^{10}Be concentrations.

For stream sediment samples, average elevation was used to calculate the average ^{10}Be production rate within each subcatchment. Equation 9 gives the spatially-averaged maximum denudation rate of the catchment above the sampling point (referred as spatially-averaged d_{max}). This calculation is based on steady-state ^{10}Be concentrations at the catchment scale and on the other assumptions stated in the introduction (assumptions 1 to 6). Finally, spatially-averaged d_{max} obtained from stream sediments can be used to determine subcatchment maximum denudation rates between two sampling points (Granger et al., 1996):

$$d_{max\ subcatchment} = \frac{d_{max,2}A_2 - d_{max,1}A_1}{A_2 - A_1} \qquad (10)$$

with A_2 and A_1 the areas of downstream and upstream catchments, respectively.

One of the important issue for the calculation of d_{max} from equation 9 is the choice of density of the eroding material. Apart for the case of granitic tors, for which the density of 2.7 g.cm^{-3} is relatively obvious, several possibilities arise for topsoil and stream sediment samples. One possibility is to use the current average densities of topsoil (≈1 g.cm^{-3}, as in Meyer et al., 2010) and of stream sediment samples (≈2.2 g.cm^{-3}) for the calculation of local and spatially-averaged d_{max}. Another approach is to use the current average density of regolith (≈1.7 g.cm^{-3}) for both cases, arguing that this density could be a better estimate for the available erodible materials at the surface. However, it must be recalled that the assumption of steady-state ^{10}Be concentrations implies a long time of cosmic ray exposure ($t \gg T_{eff}$) and this point must be kept in mind for the choice of densities. If soils are young and thin, and if most of the ^{10}Be accumulation occurs in the deeper regolith or in the bedrock, using lower density values measured from topsoils is biasing the denudation rates inferred from equation 9 toward higher values. A strategy more coherent with this assumption is to use the bedrock density (2.7 g.cm^{-3}) for all calculations. This reflects that at longer timescales, all the surface processes (soil development during interglacial and soil scraping during glacial times) are averaged out and what is eroding is in effect the underlying bedrock. We quantitatively evaluate these three approaches bellow.

6. Modeling results

6.1 Evolution, exposure age and denudation rates of depth profiles

Modeled soil production rates are variable between profiles and tend to increase with decreasing elevation (from P1 to P2 and P3, adjusted parameters in table S3). By contrast, regolith production rates are much lower in profiles P2 and P3 due to the thicker regolith already present at the initial state (table S3). Modeled soil thicknesses rapidly increase during the first 5 kyr before reaching more stable values after 10 kyr of simulation time (illustration for profile P1 in figure 4). Soil thicknesses at present time reach 50 cm for P1 and 75 cm for P2 and P3 in accordance with measurements. Final simulated bulk and integrated densities are also consistent with measurements from all depth profiles (figures 4a, 4b, 5a, 5b, 6a and 6b).

The best agreement between modeled and measured ^{10}Be concentrations are obtained with the same cosmic ray exposure age of 19 kyr, the same muonic pre-exposure age of 150 kyr in the bedrock, and the same denudation rate d of 22 mm.kyr^{-1} for the three depth profiles.

The ^{10}Be concentrations inherited from muons are presented in figure 4d. The best fit of data was characterized by Kling-Gupta coefficients of 0.96, 0.95 and 0.82 for P1, P2 and P3 profiles, respectively (Gupta et al., 2009). In profile P1, ^{10}Be concentrations in the bedrock and the lower regolith are well explained by the direct modeling (figure 5c). The ^{10}Be concentrations are well explained in the whole profile P1 after considering a recent soil expansion constrained by the volumetric strain index (by expanding the soil layers towards the surface; as in Ackerer et al., 2016; figure 5d). In P2 and P3 bedrock, ^{10}Be concentrations are well explained by the direct modeling, similarly to the P1 bedrock (figures 6c and 6d). Accurate fitting of ^{10}Be concentrations in P2 and P3 regolith is more challenging due to impact of mobile regolith within these profiles. Higher ^{10}Be concentrations in the mobile regolith of P2 and P3 are explained by the inherited ^{10}Be from mobile regolith pre-exposure (C_0 in table S3). Best agreements between modeled and measured ^{10}Be concentrations in P2 lower regolith are obtained with a full mixing of mobile regolith during the transport event that occurred before 19 kyr BP, implying a constant C_0 value over depth in P2 lower regolith (table S3, figure 6c). Best results in P3 lower regolith are obtained with a limited mixing of mobile regolith and a variable C_0 value over depth (table S3, figure 6d). Scattered ^{10}Be concentrations, probably due to surface mixing in P3 soil, is not described by our direct modeling approach (figure 6d).

6.2 Maximum denudation rates from topsoils, rock outcrops and stream sediments

Maximum denudation rates inferred from equation 9 are shown in figure 7 for topsoils, rock outcrops and stream sediments. For this calculation, we used a constant granite density of 2.7 g.cm^{-3} for all samples. Calculated spatially-averaged d_{max} are similar for all the stream sediments (36-40 mm.kyr^{-1}), apart from the sediments collected at the outlet that indicate higher denudation rate (43 mm.kyr^{-1}, table 2, figure 7a). The highest spatially-averaged d_{max} (56 mm.kyr^{-1}) is calculated for the closest subcatchment to the watershed outlet (equation 10, figure 7a). Local d_{max} for rock outcrops are lower (30-34 mm.kyr^{-1}), while local d_{max} for soils range between 30 and 42 mm.kyr^{-1} with higher denudation near the crests (figure 7a). Local d_{max} calculated for topsoil samples independently collected at the surface of depth profiles (34-42 mm.kyr^{-1}) are approximately two times higher than the denudation rate d determined from the direct modeling of the high-resolution depth profiles (22 mm.kyr^{-1}). Other choices of density for topsoil and stream sediment samples (i.e. section 5.2) increase the biases observed between the local d_{max} determined on depth profiles and the denudation rate d determined on the same depth profiles from the direct modeling (from a factor three to four).

We find no relation between catchment mean slope orientations and denudation rates (figure 7b, data in table S4), suggesting a limited role of differences in freezing-thaw cycles between north facing and south facing slopes. There is also no clear relation between catchment mean slopes and denudation rates (figure 7c, table S4): similar d_{max} are obtained for catchments with moderate mean slopes (12-18°) and only above a threshold of around 20° higher denudation is observed for the outlet subcatchment (figure 7b and table S4).

7. Discussion

7.1 Origin of mobile regolith

Our study on the Strengbach watershed indicates that two different types of mobile regolith can occur along a slope: (1) a deep mobile regolith able to transport the soil and the lower regolith and (2) a near surface mobile regolith generating an expansion or a mixing of soil layers.

For the deep mobile regolith, modeling results obtained for the three depth profiles indicate that regolith mobilization occurred around the last glacial maximum (LGM, around 24-19 kyr). The homogenization of mobile regolith was total (in P2) or partial (in P3) during transport, and stabilization occurred along the slope around 19 kyr BP. Given the moderate slopes around the three depth profiles (10-12°), the probable lack of vegetation and the prevalence of cold conditions at the elevation of the Strengbach watershed during the LGM (Leroy et al., 2000; Heyman et al., 2013), the transport of deep mobile regolith is probably explained by periglacial solifluction and cryoturbation processes. Studies of periglacial processes in present day cold environments indicate that rock debris can be transported at velocities up to 10-50 cm.yr^{-1} (Kääb and Vollmer, 2000; Wangensteen et al., 2006). With a similar downward velocity during the LGM, the distance of 200 m between P1, P2 and P3 profiles would be covered by rock debris in only 400-2000 years. These estimates indicate that the transport of mobile regolith in a periglacial context can be fast compared to the ^{10}Be production timescale, explaining why ^{10}Be concentrations within the three profiles are well modeled by the same exposure age of 19 kyr.

Study of creeping velocity for regolith particles in a warmer and drier environment was conducted by Heimsath et al. (2002). Much slower velocity was inferred for the downward migration of regolith particles by processes analogous to diffusive erosion (6 et 12 m.kyr^{-1}; Heimsath et al., 2002). By taking a mean velocity of 10 m.kyr^{-1}, 19 kyr would be needed for regolith particles to cover the distance of 200 m between P1, P2 and P3 profiles. This time is too long and incompatible with the similar ^{10}Be concentrations observed in the upper part of all profiles (table 1) and with the modeling results pointing to a similar exposure age across the slope (table S3). Therefore, the deep mobile regolith observed in the watershed is most likely explained by rapid peri-glacial processes occurring during the LGM (episodic erosion;

Norton et al., 2010), and not by continuous creeping as suggested in other mountain catchments (West et al., 2013).

In contrast, the near surface (< 1 m of depth) regolith mobility is probably a recent mechanism (Holocene to actual). A longer cosmic ray exposure of a stable profile would inexorably produce a simple exponential decrease of ^{10}Be concentrations with depth, which is not observed in P2 and P3. Given the moderate slopes and the dense forest cover currently present around the depth profiles, recent erosion processes are probably dominated by diffusive erosion (Montgomery and Brandon, 2002) and soil layers are likely impacted by biological processes (Wilkinson et al., 2009). In P1, the linear trend of ^{10}Be concentrations observed in the soil is explained by the volumetric expansion due to the incorporation of organic matter (Ackerer et al., 2016). In P2 and P3, the soil mixing appears incomplete, as ^{10}Be concentrations are not homogenized over depth as illustrated by Dixon and Riebe (2014). This soil mixing is likely related to recent diffusive erosion, bioturbation by living organisms, tree throw, or anthropogenic perturbations during the last centuries (Etienne et al., 2013).

The differences between superficial and deep mobile regolith are rarely discussed in the literature (e.g. Dixon and Riebe., 2014; Schaller et al., 2018). One reason is that most of studies investigated shallower depth profiles or that sampling resolution in the deeper part of depth profiles is too low to highlight complex ^{10}Be concentration trends and the presence of deep mobile regolith. We therefore emphasize the importance of a high-resolution sampling in the lower part of depth profiles to identify deep mobile regolith and to better constrain the long-term evolution of the regolith along hillslopes.

7.2 Role of mobile regolith in CZ evolution

Our data and modeling results indicate that the mobile regolith has a key role in the CZ evolution as it modifies and complexifies the CZ structure (summary figure 8). Firstly, the occurrence of deep mobile regolith implies a disconnection between the bedrock in place and the regolith. This induces a greater heterogeneity, explaining the sharper variations of mineralogical and chemical composition at the bedrock/regolith interface within P2 and P3 profiles (figure 2). The deep mobile regolith also modifies the inherited ^{10}Be concentrations (figures 3 and 8), increasing ^{10}Be concentrations in the regolith of profiles located downslope (P2 and P3).

The deep mobile regolith also impacts soil and regolith production rates. Higher soil formation rates from lower regolith weathering are modeled in P2 and P3 profiles (section 5.2), and thicker and more evolved soils (ochric podzols) are observed within profiles developed on a deep mobile regolith (figures 1 and 8). These points are potentially explained by a faster weathering of the transported material found in the mobile regolith compared to the direct weathering of a lower regolith in place. By contrast, modeled values of regolith production rates from bedrock weathering are faster at the summit (P1) than at lower elevation along the hillslope (P2 and P3).

Ma et al. (2010) focused on a watershed affected by periglacial processes and based on U-series isotopes also concluded that regolith production rates decrease with increasing regolith thickness and distance from the crests. Our results support this scheme and show that one possible explanation of this functioning is the deposition of mobile regolith along slopes. In fact, this process is explaining both the thickening of regolith at lower elevation and the protection of bedrock from weathering, which reduces regolith production rate.

The deep mobile regolith has also implications on the hydrological processes and water storage across landscape. It induces a thickening of weathered material in the lower parts of the watershed, which tends to enhance water storage capacity. Higher water storage capacity at mid-slope locations compared to crests was identified as an important feature to correctly model the hydrogeochemical functioning of the watershed (Weill et al., 2019; Ackerer et al., 2020a).

Many studies investigating the CZ evolution pictured that the mobile regolith is relatively superficial, affecting soils, and implying an almost complete mixing of soil layers (e.g. Anderson et al., 2007; Dixon and Von Blanckenburg, 2012; Riebe et al., 2017; Schaller et al., 2018). If a near surface mobile regolith is typically identified, the deep mobile regolith extending below the soil is too often neglected to understand the CZ structure and its evolution. As shown by the detailed modeling of depth profiles, the deep mobile regolith is not always well mixed, suggesting that a depth dependent transport law as proposed by Heimsath et al. (2005) is also valid in the context of shallow gradient slopes of watersheds affected by periglacial processes. The mobile regolith may also change the relationship between physical erosion and chemical denudation rates across landscape, by complexifying the idealized soil mantled hillslope where soil is directly produced from bedrock weathering (e.g. Ferrier and Kirchner; 2008).

7.3 Impact of the assumption of steady-state ^{10}Be concentrations on denudation rates

The results show that the denudation rate d (22 mm.kyr^{-1}) determined from the direct modeling of depth profiles without any steady-state assumption on ^{10}Be concentrations is approximately two times lower than the local d_{max} (34-42 mm.kyr^{-1}, figure 7a) calculated on the same profiles with independent topsoil samples. This bias rises to a factor of three or even four when considering current average regolith or topsoil densities (≈1.7 g.cm^{-3} and ≈1 g.cm^{-3} respectively) instead of the bedrock density (2.7 g.cm^{-3}) in the calculation of local d_{max}.

This bias is explained by the fact that in the Strengbach catchment, the ^{10}Be concentrations are currently not at steady-state, i.e. production, denudation and radioactive decay are not balanced. Additional simulations were performed on the profiles for the next 5,000 or 10,000 years, indicating a significant increase in ^{10}Be concentrations in the soil, regolith and bedrock for all depth profiles. Such behavior is related to the short cosmic ray exposure age of the regolith. Calculation of the effective irradiation time (T_{eff}) indicates that the exposure age should be longer than 40-50 kyr to validate the assumption of steady-state ^{10}Be concentrations, which is not the case given the important erosion event that affected the profiles at around 19 kyr BP (i.e. $t < T_{eff}$).

A key finding is that the depth profiles, although not in steady-state for the ^{10}Be concentrations, are close to a steady-state for their soil and regolith thicknesses (figure 4). The simulated regolith production rates are close to the simulated denudation rates within the Holocene timeframe. This conclusion is supported by the observation that our simulated regolith production rate in P1 (approximately 14 mm.kyr^{-1} over the last 15 kyr, table S3) is consistent with the regolith production rate independently determined on the millennial timescale from U-Th-Ra isotopes (approximately 12 mm.kyr^{-1}, Ackerer et al., 2016).

We also highlight the importance of considering soil expansion (non-isovolumetric weathering) when deciphering the evolution of depth profiles. In P1, a steady-state of regolith thickness and mass balance has been reached with a regolith production rate of 12 mm.kyr^{-1} and a denudation rate of 22 mm.kyr^{-1}: the weathering of a given thickness of bedrock produces approximately twice more thickness of soil due to the volumetric expansion and the decrease in density. When considering the differences in density and expansion processes, regolith production and denudation rates expressed in specific mass fluxes are in fact similar in P1 (30±10 and 37±15 $T.km^{-2}.yr^{-1}$, respectively; Ackerer et al., 2016).

We therefore advocate for a clear distinction between two different equilibrium states: a steady sate of ^{10}Be concentrations achieved when ^{10}Be production is balanced by denudation and radioactive decay, and a steady-state of regolith thickness (or mass balance) reached when regolith production is balanced by total denudation. Our results demonstrate that these two steady-states are not necessarily reached over the same timescale. In the case of the Strengbach watershed and nearby the crests, the steady-state of regolith thickness is reached before that of the ^{10}Be concentrations.

One way to correct the bias induced by the assumption of steady-state ^{10}Be concentrations on the local d_{max} is to rather estimate denudation rates d from equation 4, at z=0, using the inherited ^{10}Be concentrations and the exposure age both deduced from the modeling of high-resolution depth profiles. The determination of these corrected denudation rates d can be done with a numerical inverse procedure (Ackerer et al., 2016), by minimizing the difference between ^{10}Be concentrations measured in samples and ^{10}Be concentrations calculated from equation 4.

On our depth profiles, the corrected local d from topsoil samples indicate that denudation rates range between 33 $mm.kyr^{-1}$ (in P1) and 14 $mm.kyr^{-1}$ (in P2), much more consistent with the value of 22 $mm.kyr^{-1}$ estimated by the direct modeling of depth profiles (table 2). We used for this calculation the average regolith density of 1.7 $g.cm^{-3}$, as this density is representative of the eroded regolith during the time-window from 19 kyr BP to present. The scattering of the revised denudations is certainly affected by the mixing processes of the shallow samples. Even though the corrected denudation values are only calculated for 3 samples, it is interesting to note that the average of these three d values is 22 mm.kyr^{-1}, i.e. identical within error to the value derived from the modelling of depth profiles. This result is consistent with the classical approach that recommends averaging the denudation rates of several samples for a given area, rather than relying on a single sample estimate.

The bias induced by the classical assumption of steady-state ^{10}Be concentrations (an overestimation of local denudation rates by a factor two to four) has probably a limited consequence for studies dealing with first-order estimates of denudation rates and/or comparing several watersheds with very different denudation rates. However, this bias is significant for studies attempting to better understand the geomorphological evolution of a watershed, as for example studies comparing local denudation of ridge crests with watershed-scale averaged denudation (e.g. Meyer et al., 2010). Our study shows that the assumption of steady-state ^{10}Be concentrations should be used very carefully in mountain environments where regoliths with short cosmic ray exposure ages are present. Combining high-resolution depth profiles with local regolith and topsoil samples is a way to quantify the impact of this assumption on denudation estimates.

7.4 Spatiotemporal variability of denudation rates and geomorphological implications

The temporal variability of denudation can firstly be estimated from the direct modeling of depth profiles. Denudation rates likely strongly decreased between the LGM and the last 19 kyr, as indicated by the cosmic ray exposure age of depth profiles pointing to important erosion events before 19 kyr BP and a period of relative stability after 19 kyr BP (figure 8). A second comparison can be made from the modern measurements of denudation. The research conducted in the Strengbach watershed shows that the current denudation determined from solute and solid fluxes at the outlet (around 15 $T.km^{-2}.yr^{-1}$, with 5 $T.km^{-2}.yr^{-1}$ of solute exports and 10 $T.km^{-2}.yr^{-1}$ of solid exports over 20 yr of record; Viville et al., 2012; Cotel et al., 2016; Ackerer et al., 2020) is lower than the long-term denudation inferred from ^{10}Be data (around 37 $T.km^{-2}.yr^{-1}$, determined on the last 19 kyr on P1; Ackerer et al., 2016). A general trend of denudation decrease with time is then highlighted from the LGM to the last 19 kyr, and from this 19 kyr time-window to present. A probable explanation is the progressive development of vegetation during the Holocene at this elevation (Leroy et al., 2000), and the dense forest cover observed today in the watershed (Pierret et al., 2018). Another explanation which cannot be excluded is that modern measurements were not affected by rare but high magnitude erosion events, as suggested by Kirchner et al. (2001).

The spatial variability of denudation can be discussed by the comparison of denudations rates determined from depth profile, topsoil, rock outcrop and stream sediment samples. As discussed in section 7.3, the assumption of steady-state ^{10}Be concentrations is not applicable for these sites. This suggests that the same assumption is probably too strong for the determination of denudation rates from other soil, outcrop, or sediment samples in the watershed and that the determined d_{max} values are biased. The approach to correct theses estimates developed in section 7.3 has been applied for these different samples to estimate more realistic denudation rates from ^{10}Be concentrations. For all the Strengbach samples, a corrected denudation rate d has been determined by numerical inverse procedure from equation 4, with the assumption that the entire watershed is characterized by the same exposure age and the same inherited ^{10}Be concentration as established on depth profiles.

Comparison of corrected denudation rates inferred from topsoil, rock outcrop and stream sediment samples allows for a detailed understanding of the evolution of the watershed geomorphology (figure 9, table 2). On the upper part of the watershed, lower denudation rates on rock outcrops compared to soil and sediment denudation rates indicate an ongoing individualization and growth of bare rocks. The observation that rock outcrops have lower denudation rates than other parts of the basin is classically invoked to explain the prominence of these structures in the landscape (Riebe et al., 2003; Heimsath et al., 2010). With denudation rates of around 22 mm.kyr^{-1} for the regolith and 4 to 9 mm.kyr^{-1} for the tors, in 19 kyr the topographic difference between the soil surface and tors would be a few tens of cm, consistent with field observations for the STR 11-1 site. However, these values are far too low to explain the morphologies observed at site STR11-5 where the bedrock outcrop surface overhangs the surrounding soils by nearly 2 m. With the estimated denudation rates presented above, such topographic differences would require nearly 150 kyr to be obtained, i.e. the time of the penultimate strong denudation event of the site based on the interpretations of Ackerer et al. (2016). We therefore propose that bedrock outcrops in these areas result from their exposure during stripping events of locally resistant bedrock portions, accounting for denudation at lower rates in these areas compared to other rocks. This interpretation remains to be validated by detailed studies of these tors, which is beyond the scope of this study.

It can also be noted that in the upper part of the watershed, the highest local denudation rates are observed on the crests (33-36 mm.kyr^{-1}), with values significantly higher than the local rate determined above the main catchment knickpoint (i.e. STR11-7; 12 mm.kyr^{-1}; figure 9). By comparing corrected spatially-averaged d from sediments from the upper part of the stream with corrected local d from soils on crests (as in Meyer et al., 2010), the relief decrease between the crests and above the river knickpoint would be around 15 mm.kyr^{-1}. However, it must be noted that this relief variation is close to uncertainties, if we consider the substantial variability of local denudation rates determined near the crest at the surface of depth profiles (33-14 mm.kyr^{-1}; figure 9). Therefore, except the significant topographic growth of local granitic outcrops, the upper part of the watershed is likely affected by a limited relief variation.

This is clearly in contrast with the variability of denudation rates at the scale of the entire watershed. The lower part of the watershed stands out from the rest of the watershed, as the highest denudation rate in the whole watershed is undeniably determined for the outlet subcatchment (99 mm.kyr^{-1}, figure 9). With the above assumptions (i.e. same exposure age and inherited ^{10}Be for the entire watershed), the high denudation rate of the outlet subcatchment compared to the ones determined from the sediments collected in the upper part of the stream (23-18 mm.kyr^{-1}) implies that a regressive erosion from the bottom of the valley steepens the topography nearby the stream outlet. By comparing corrected spatially-averaged d in the outlet subcatchment with corrected local d from soils on crests, the total watershed relief increase would be around 65 mm.kyr^{-1}, following the approach given in Meyer et al. (2010). From the above discussion, it can also be proposed that the Strengbach watershed is subdivided into two different geomorphological systems, with an upper part with a nearly constant relief and a lower part characterized by a relief increase localized near the stream incision.

Different quantitative estimates would be determined for the geomorphological evolution of the watershed from denudation rates uncorrected or differently corrected. The lowest relief change between crests and outlet would be obtained with uncorrected denudation rates

(≈20 mm.kyr^{-1}, figures 7). But from a qualitative point of view this would not change the conclusion that the Strengbach watershed is marked by a noticeable spatial variability of its denudation with an upstream subcatchment with limited relief change and a downstream one with a localized regressive denudation near the stream outlet. The Strengbach case therefore illustrates that even in a watershed where the steady-state assumption of ^{10}Be concentrations is not verified ($t < T_{eff}$), the spatial variations of in-situ ^{10}Be concentrations in sediments still carry qualitatively relevant information on the geomorphological evolution of landscapes.

8. Conclusion

We presented in this study a rare combination of in-situ ^{10}Be data from high resolution depth profiles, soils, rock outcrops and stream sediments in a small mountain watershed. The high resolution of depth profile sampling was a key point to understand how the mobile regolith is generated and how it affects the CZ evolution (summary figure 8). Two different types of mobile regolith were identified: a deep mobile regolith explained by periglacial processes exclusively occurring during the LGM and a superficial mobile regolith generating a recent expansion or mixing of soil layers. Deep mobile regolith clearly modifies ^{10}Be concentrations and mineralogical, geochemical and physical evolution of the CZ. The modeling of regolith evolution and of ^{10}Be concentrations along depth allows to estimate the cosmic ray exposure age (19 kyr) and the mean denudation rate (22 mm.kyr^{-1}) of high-resolution depth profiles without any assumption of steady-state ^{10}Be concentrations. Comparison with maximum denudation rates inferred from topsoil samples independently collected at the surface of depth profiles and interpreted under the assumption of steady-state ^{10}Be concentrations shows that this assumption leads to an overestimation of local denudation rates by a factor of approximately two. One important conclusion of our study is to show that if one wants to estimate denudation rates by following the classical approach (i.e. single topsoil sample, assumption of steady-state ^{10}Be concentrations), the best estimates are obtained when using the density of the bedrock. Results also indicate that maximum spatially-averaged denudation rates determined from stream sediment samples overestimate denudation rates by a factor of approximately two. These biases are significant to understand the precise geomorphological evolution of a watershed, and we propose a method to estimate corrected denudation rates. The comparison between corrected local and spatially-averaged denudation rates indicates that the watershed geomorphology is evolving and that regressive erosion increases the relief nearby the outlet. A key finding is also that a steady-state of ^{10}Be concentrations and a steady-state of regolith thickness (or mass balance) are two different situations that do not necessarily overlap. In the case of the Strengbach watershed crests, a steady-state of ^{10}Be concentrations is not achieved while regolith thickness tends to a steady-state. However, even in a watershed where the steady-state assumption of ^{10}Be concentrations is not verified ($t < T_{eff}$), the spatial variations of in-situ ^{10}Be concentrations in sediments still provide relevant information on the geomorphological evolution of landscapes.

Bibliography

Ackerer, J., Chabaux, F., Van der Woerd, J., Viville, D., Pelt, E., Kali, E., Lerouge, C., Ackerer, P., di Chiara Roupert, R., & Négrel, P. (2016). Regolith evolution on the millennial timescale from combined U–Th–Ra isotopes and in-situ cosmogenic 10Be analysis in a weathering profile (Strengbach catchment, France). *Earth and Planetary Science Letters*, *453*, 33-43.

Ackerer, J., Jeannot, B., Delay, F., Weill, S., Lucas, Y., Fritz, B., Beaulieu, E., Viville, D., Pierret, M.C., Gangloff, S., & Chabaux, F. (2020). Crossing hydrological and geochemical modeling to understand the spatiotemporal variability of water chemistry in a headwater catchment (Strengbach, France). *Hydrology and Earth System Sciences*, *24*(6), 3111-3133.

Anderson, S. P., von Blanckenburg, F., & White, A. F. (2007). Physical and chemical controls on the critical zone. *Elements*, *3*(5), 315-319.

Braucher, R., Del Castillo, P., Siame, L., Hidy, A. J., & Bourles, D. L. (2009). Determination of both exposure time and denudation rate from an in-situ-produced 10Be depth profile: a mathematical proof of uniqueness. Model sensitivity and applications to natural cases. *Quaternary Geochronology*, *4*(1), 56-67.

Brimhall, G. H., Ford, C., Bratt, J., Taylor, G., & Warin, O. (1991). Quantitative geochemical approach to pedogenesis: importance of parent material reduction, volumetric expansion, and eolian influx in lateritization. *Geoderma*, *51*(1), 51-91.

Brown, E. T., Stallard, R. F., Larsen, M. C., Raisbeck, G. M., & Yiou, F. (1995). Denudation rates determined from the accumulation of in-situ-produced 10Be in the Luquillo Experimental Forest, Puerto Rico. *Earth and Planetary Science Letters*, *129*(1-4), 193-202.

Chabaux, F., Viville, D., Lucas, Y., Ackerer, J., Ranchoux, C., Bosia, C., Pierret, M. C., Labasque, T., Aquilina, L., Wyns, R., Lerouge, C., Dezaye, C., & Négrel, P. (2017). Geochemical tracing and modeling of surface and deep water–rock interactions in elementary granitic watersheds (Strengbach and Ringelbach CZOs, France). *Acta Geochimica*, *36*(3), 363-366.

Chabaux, F., Stille, P., Prunier, J., Gangloff, S., Lemarchand, D., Morvan, G., Négrel, J., Pelt, Pierret, M.C., Rihs, S., Schmitt, A.S., Trémolières, M., & Viville, D. (2019). Plant-soil-water interactions: Implications from U-Th-Ra isotope analysis in soils, soil solutions and vegetation (Strengbach CZO, France). *Geochimica et Cosmochimica Acta*, *259*, 188-210.

Charreau, J., Blard, P. H., Zumaque, J., Martin, L. C., Delobel, T., & Szafran, L. (2019). Basinga: A cell-by-cell GIS toolbox for computing basin average scaling factors, cosmogenic production rates and denudation rates. *Earth Surface Processes and Landforms*, *44*(12), 2349-2365.

Codilean, A. T. (2006). Calculation of the cosmogenic nuclide production topographic shielding scaling factor for large areas using DEMs. *Earth Surface Processes and Landforms*, *31*(6), 785-794.

Cotel, S., Viville, D., Pierret, M. C., Benarioumlil, S., & Chabaux, F. (2016, April). Evaluation of fluxes of suspended matters and bedload in the small granitic Strengbach catchment (Vosges massif, France). In *EGU General Assembly Conference Abstracts* (pp. EPSC2016-13179).

Dixon, J. L., & Riebe, C. S. (2014). Tracing and pacing soil across slopes. *Elements*, *10*(5), 363-368.

Dixon, J. L., & von Blanckenburg, F. (2012). Soils as pacemakers and limiters of global silicate weathering. *Comptes Rendus Geoscience*, *344*(11-12), 597-609.

Dongen, R. V., Scherler, D., Wittmann, H., & Blanckenburg, F. V. (2019). Cosmogenic 10 Be in river sediment: where grain size matters and why. *Earth Surface Dynamics*, *7*(2), 393-410.

Dunai, T. J. (2010). *Cosmogenic nuclides: principles, concepts and applications in the earth surface sciences*. Cambridge University Press.

Egli, M., Dahms, D., & Norton, K. (2014). Soil formation rates on silicate parent material in alpine environments: Different approaches–different results?. *Geoderma*, *213*, 320-333.

Etienne, D., Ruffaldi, P., Dupouey, J. L., Georges-Leroy, M., Ritz, F., & Dambrine, E. (2013). Searching for ancient forests: A 2000 year history of land use in northeastern French forests deduced from the pollen compositions of closed depressions. *The Holocene*, *23*(5), 678-691.

Fichter, J., Turpault, M. P., Dambrine, E., & Ranger, J. (1998). Mineral evolution of acid forest soils in the Strengbach catchment (Vosges mountains, NE France). *Geoderma*, *82*(4), 315-340.

Foster, M. A., Anderson, R. S., Wyshnytzky, C. E., Ouimet, W. B., & Dethier, D. P. (2015). Hillslope lowering rates and mobile-regolith residence times from in-situ and meteoric 10Be analysis, Boulder Creek Critical Zone Observatory, Colorado. *Bulletin*, *127*(5-6), 862-878.

Gangloff S., Stille P., Pierret M-C., Weber T., Chabaux F. (2014) Characterization and evolution of dissolved organic matter in acidic forest soil and its impact on the mobility of major and trace elements (case of the Strengbach watershed) Geochimica et Cosmochimica Acta, 130, 21-41.

Granger, D. E., Kirchner, J. W., & Finkel, R. (1996). Spatially averaged long-term erosion rates measured from in-situ-produced cosmogenic nuclides in alluvial sediment. *The Journal of Geology*, *104*(3), 249-257.

Gupta, H. V., Kling, H., Yilmaz, K. K., & Martinez, G. F. (2009). Decomposition of the mean squared error and NSE performance criteria: Implications for improving hydrological modelling. *Journal of hydrology*, *377*(1-2), 80-91.

Heyman, B. M., Heyman, J., Fickert, T., & Harbor, J. M. (2013). Paleo-climate of the central European uplands during the last glacial maximum based on glacier mass-balance modeling. Quaternary Research, 79(1), 49-54.

Heimsath, A. M., Dietrich, W. E., Nishiizumi, K., & Finkel, R. C. (1997). The soil production function and landscape equilibrium. *Nature*, *388*(6640), 358-361.

Heimsath, A. M., Chappell, J., Spooner, N. A., & Questiaux, D. G. (2002). Creeping soil. *Geology*, *30*(2), 111-114.

Heimsath, A. M., Furbish, D. J., & Dietrich, W. E. (2005). The illusion of diffusion: Field evidence for depth-dependent sediment transport. *Geology*, *33*(12), 949-952.

Heimsath, A. M., Chappell, J., & Fifield, K. (2010). Eroding Australia: rates and processes from Bega Valley to Arnhem land. *Geological Society, London, Special Publications*, *346*(1), 225-241.

Hidy, A. J., Gosse, J. C., Sanborn, P., & Froese, D. G. (2018). Age-erosion constraints on an Early Pleistocene paleosol in Yukon, Canada, with profiles of 10Be and 26Al: Evidence for a significant loess cover effect on cosmogenic nuclide production rates. *Catena*, *165*, 260-271.

Kääb, A., & Vollmer, M. (2000). Surface geometry, thickness changes and flow fields on creeping mountain permafrost: automatic extraction by digital image analysis. *Permafrost and Periglacial Processes*, *11*(4), 315-326.

Kirchner, J. W., Finkel, R. C., Riebe, C. S., Granger, D. E., Clayton, J. L., King, J. G., & Megahan, W. F. (2001). Mountain erosion over 10 yr, 10 ky, and 10 my time scales. *Geology, 29*(7), 591-594.

Kohl, C. P., & Nishiizumi, K. (1992). Chemical isolation of quartz for measurement of in-situ-produced cosmogenic nuclides. *Geochimica et Cosmochimica Acta*, *56*(9), 3583-3587.

Larsen, I. J., Almond, P. C., Eger, A., Stone, J. O., Montgomery, D. R., & Malcolm, B. (2014). Rapid soil production and weathering in the Southern Alps, New Zealand. *Science*, *343*(6171), 637-640.

Leroy, S. A. G., Zolitschka, B., Negendank, J. F. W., & Seret, G. (2000). Palynological analyses in the laminated sediment of Lake Holzmaar (Eifel, Germany): duration of Lateglacial and Preboreal biozones. *Boreas*, *29*(1), 52-71.

Lupker, M., France-Lanord, C., Galy, V., Lavé, J., Gaillardet, J., Gajurel, A. P., Guilmette, C., Rahman, M., Singh, S.K., & Sinha, R. (2012). Predominant floodplain over mountain weathering of Himalayan sediments (Ganga basin). *Geochimica et Cosmochimica Acta*, *84*, 410-432.

Ma, L., Chabaux, F., Pelt, E., Blaes, E., Jin, L., & Brantley, S. (2010). Regolith production rates calculated with uranium-series isotopes at Susquehanna/Shale Hills Critical Zone Observatory. *Earth and Planetary Science Letters*, *297*(1-2), 211-225.

Mariotti, A., Blard, P. H., Charreau, J., Petit, C., Molliex, S., & ASTER Team. (2019). Denudation systematics inferred from in situ cosmogenic 10 Be concentrations in fine (50–100 µm) and medium (100–250 µm) sediments of the Var River basin, southern French Alps. *Earth Surface Dynamics*, *7*(4), 1059-1074.

Martin, L. C. P., Blard, P. H., Balco, G., Lavé, J., Delunel, R., Lifton, N., & Laurent, V. (2017). The CREp program and the ICE-D production rate calibration database: A fully parameterizable and updated online tool to compute cosmic-ray exposure ages. *Quaternary geochronology*, *38*, 25-49.

Mercier, J. L., Bourlès, D. L., Kalvoda, J., Braucher, R., & Paschen, A. (1999). Deglaciation of the Vosges dated using 10Be. *Acta Universitatis Carolinae–Geographica*, *2*, 139-155.

Meyer, H., Hetzel, R., Fügenschuh, B., & Strauss, H. (2010). Determining the growth rate of topographic relief using in-situ-produced 10Be: A case study in the Black Forest, Germany. *Earth and Planetary Science Letters*, *290*(3-4), 391-402.

Montgomery, D. R., & Brandon, M. T. (2002). Topographic controls on erosion rates in tectonically active mountain ranges. *Earth and Planetary Science Letters*, *201*(3-4), 481-489.

Norton, K. P., von Blanckenburg, F., & Kubik, P. W. (2010). Cosmogenic nuclide-derived rates of diffusive and episodic erosion in the glacially sculpted upper Rhone Valley, Swiss Alps. Earth Surface Processes and Landforms, 35(6), 651-662.

Pierret, M. C., Cotel, S., Ackerer, P., Beaulieu, E., Benarioumlil, S., Boucher, M., Boutin, R., Chabaux, F., Delay, F., Fourtet, C., Friedmann, P., Fritz, B., Gangloff, S., Girard, J-F., Legtchenko, A., Viville, D., Weill, S., & Probst, A. (2018). The Strengbach catchment: A multidisciplinary environmental sentry for 30 years. *Vadose Zone Journal*, *17*(1), 1-17.

Portenga, E. W., & Bierman, P. R. (2011). Understanding Earth's eroding surface with 10 Be. GSA. 4-10.

Prunier, J., Chabaux, F., Stille, P., Pierret, M.C., Viville, D., Gangloff, S. (2015) Monitoring of geochemical and isotopic (Sr,U) signatures in soil solutions for the evaluation of soil weathering evolution (the Strengbach case) *Chemical Geology, 417*, 289–305.

Ranchoux, C., Chabaux, F., Viville, D., Labasque, T., Lucas, Y., Van Der Woerd, J., Ackerer, J., & Aquilina, L. (2021). Characterization of groundwater circulations in a headwater catchment from an analysis of chemical concentrations, Sr-Nd-U isotope ratios, and CFC, SF6 gas tracers (Strengbach CZO, France). Applied Geochemistry, 131, 105030.

Riebe, C. S., Kirchner, J. W., & Finkel, R. C. (2003). Long-term rates of chemical weathering and physical erosion from cosmogenic nuclides and geochemical mass balance. *Geochimica et Cosmochimica Acta*, *67*(22), 4411-4427.

Riebe, C. S., Hahm, W. J., & Brantley, S. L. (2017). Controls on deep critical zone architecture: A historical review and four testable hypotheses. *Earth Surface Processes and Landforms*, *42*(1), 128-156.

Schaller, M., Blanckenburg, F. V., Hovius, N., Veldkamp, A., van den Berg, M. W., & Kubik, P. W. (2004). Paleoerosion rates from cosmogenic 10Be in a 1.3 Ma terrace sequence: response of the River Meuse to changes in climate and rock uplift. *The Journal of geology*, *112*(2), 127-144.

Schaller, M., Ehlers, T. A., Lang, K. A., Schmid, M., & Fuentes-Espoz, J. P. (2018). Addressing the contribution of climate and vegetation cover on hillslope denudation, Chilean Coastal Cordillera (26–38 S). *Earth and Planetary Science Letters*, *489*, 111-122.

Schoonejans, J., Vanacker, V., Opfergelt, S., Granet, M., & Chabaux, F. (2016). Coupling uranium series and 10Be cosmogenic radionuclides to evaluate steady-state soil thickness in the Betic Cordillera. *Chemical Geology*, *446*, 99-109.

Siame, L., Bellier, O., Braucher, R., Sébrier, M., Cushing, M., Bourlès, D., & Yiou, F. (2004). Local erosion rates versus active tectonics: cosmic ray exposure modelling in Provence (south-east France). *Earth and Planetary Science Letters*, *220*(3), 345-364.

Stone, J. O. (2000). Air pressure and cosmogenic isotope production. *Journal of Geophysical Research: Solid Earth*, *105*(B10), 23753-23759.

Vanacker, V., von Blanckenburg, F., Govers, G., Molina, A., Poesen, J., Deckers, J., & Kubik, P. (2007). Restoring dense vegetation can slow mountain erosion to near natural benchmark levels. *Geology*, *35*(4), 303-306.

Viville, D., Chabaux, F., Stille, P., Pierret, M. C., & Gangloff, S. (2012). Erosion and weathering fluxes in granitic basins: the example of the Strengbach catchment (Vosges massif, eastern France). *Catena*, *92*, 122-129.

Von Blanckenburg, F. (2005). The control mechanisms of erosion and weathering at basin scale from cosmogenic nuclides in river sediment. *Earth and Planetary Science Letters*, *237*(3-4), 462-479.

Wangensteen, B., Guðmundsson, Á., Eiken, T., Kääb, A., Farbrot, H., & Etzelmüller, B. (2006). Surface displacements and surface age estimates for creeping slope landforms in Northern and Eastern Iceland using digital photogrammetry. *Geomorphology*, *80*(1-2), 59-79.

Weill, S., Lesparre, N., Jeannot, B., & Delay, F. (2019). Variability of water transit time distributions at the Strengbach catchment (Vosges Mountains, France) inferred through integrated hydrological modeling and particle tracking algorithms. *Water*, *11*(12), 2637.

West, A. J. (2012). Thickness of the chemical weathering zone and implications for erosional and climatic drivers of weathering and for carbon-cycle feedbacks. *Geology*, *40*(9), 811-814.

West, N., Kirby, E., Bierman, P., Slingerland, R., Ma, L., Rood, D., & Brantley, S. (2013). Regolith production and transport at the Susquehanna Shale Hills Critical Zone Observatory, part 2: insights from meteoric 10Be. *Journal of Geophysical Research: Earth Surface*, *118*(3), 1877-1896.

Wild, B., Daval, D., Beaulieu, E., Pierret, M. C., Viville, D., & Imfeld, G. (2019). In-situ dissolution rates of silicate minerals and associated bacterial communities in the critical zone (Strengbach catchment, France). *Geochimica et Cosmochimica Acta*, *249*, 95-120.

Wilkinson, M. T., Richards, P. J., & Humphreys, G. S. (2009). Breaking ground: pedological, geological, and ecological implications of soil bioturbation. *Earth-Science Reviews*, *97*(1-4), 257-272.

Figure caption

Figure 1: study watershed and sampling location. (a) Strengbach watershed location in northeastern France. (b) Sampling location of ^{10}Be samples including topsoil, rock outcrop, stream sediment and high-resolution depth profile samples. (c) Photography of the three high-resolution depth profiles realized on the southern part of the watershed. Yellow rectangles represent collected samples of soil, regolith or bedrock. Blue diamonds represent samples for which mineralogical, geochemical and ^{10}Be analysis were performed. The profile P1 was investigated by Ackerer et al. (2016). Mor litter is defined by a thick mat of undecomposed to partially decomposed litter that is not significantly incorporated into the soil, present in coniferous forests. Moder litter is defined by an undecomposed and partially decomposed remains of broad-leaved deciduous forest litter that is shallowly incorporated into the soil.

Figure 2: chemical mobility coefficients ($\tau_i = \left(\frac{C(i)_{sample}\, C(j)_{bedrock}}{C(i)_{bedrock}\, C(j)_{sample}} - 1\right)$) for the three high-resolution depth profiles on the southern slope of the watershed. (a) Subplot for the depth profile P1. (b) Subplot for the depth profile P2. (c) Subplot for the depth profile P3.

Figure 3: ^{10}Be data, volumetric variations, and bulk density from the three high-resolution depth profiles (P1, P2 and P3). (a) ^{10}Be concentrations measured in bulk samples. (b) Volumetric strain index ($\varepsilon = \left(\frac{C(j)_{bedrock}\, \rho_{bedrock}}{C(j)_{sample}\, \rho_{sample}}\right) - 1$). (c) Bulk density.

Figure 4: direct modeling of the evolution of P1 profile. Black lines represent from top to bottom, soil surface, soil base and bedrock interfaces. (a) Bulk density evolution. (b) Integrated density evolution. (c) ^{10}Be production rate evolution. (d) ^{10}Be concentrations from muonic pre-exposure (150 kyr). Calculations of the muonic pre-exposure consider the erosion of regolith over time, and especially the important erosion event that removed approximately 2 m of regolith during the Last Glacial Maximum (Ackerer et al., 2016).

Figure 5: modeling results for the P1 profile. (a) Measured and modeled bulk density. (b) Measured and modeled integrated density. (c) Comparison between measured and simulated ^{10}Be concentrations. (d) Comparison between measured and simulated ^{10}Be concentrations including a correction of soil expansion.

Figure 6: modeling results for P2 and P3 profiles. (a) Measured and modeled integrated density for the profile 1. (b) Measured and modeled integrated density for the P2 profile. (c) Comparison between measured and simulated ^{10}Be concentrations for the P2 profile. (d) Comparison between measured and simulated ^{10}Be concentrations for the P3 profile.

Figure 7: slopes, catchments of stream sediments and spatial variability of denudation rates in the Strengbach watershed. (a) Map of the watershed. Maximal denudation rates (d_{max}) written in black are inferred from ^{10}Be concentrations measured in topsoil, rock outcrop and stream sediment samples with the GIS toolbox Basinga (Charreau et al., 2019) using equation 9 ($d_{max} \approx \left(\frac{P.P_n}{C}\right)\frac{K_n}{\rho} +$

$\left(\frac{P.P_{nm}}{C}\right)\frac{K_{nm}}{\rho}+\left(\frac{P.P_{fm}}{C}\right)\frac{K_{fm}}{\rho}$) and under the assumption of steady state ^{10}Be concentrations. A constant bedrock density of 2.7 g.cm^{-3} was used in all calculations. The denudation rate written in blue is determined through the modeling of high-resolution depth profiles without the assumption of steady state ^{10}Be concentrations (d, equation 4). The denudation rate written in bold black for the outlet subcatchment is calculated from equation 10. Denudation rates are expressed in mm.kyr^{-1} and uncertainties include the uncertainties on the ^{10}Be concentrations, blank correction, and ^{10}Be production rates (uncertainties in table 2). (b) Spatially-averaged d_{max} calculated for stream sediment catchments as a function of mean catchment aspect (° from N). (c) Spatially-averaged d_{max} calculated for stream sediment catchments as a function of mean catchment slope (°). Error bars represent one standard deviation of data.

Figure 8: summary diagram of the four major stages of the CZ evolution along the southern slope of the Strengbach watershed. Stage (1) around 25 000 BP: presence of paleo profiles with inherited in-situ ^{10}Be concentrations in the bedrock corresponding to the long term muonic exposure during approximately 150 kyr. Stage (2) around 24 000-20 000 BP: major erosion event removing the paleo profile soil and regolith in P2 and P3 but keeping in place part of the regolith in P1. Stage (3) around 19 000 BP: stabilization of deep mobile regolith on the bedrock of P2 and P3 profiles. P1 is still covered by part of the in-situ regolith. Stage (4) from 19 000 BP to present: period with lower denudation rates explaining the soil development and the exposure age of 19 000 yr determined for all profiles. In P1, a thin soil was developed from the weathering of in situ regolith and was affected by near surface mobile regolith and volumetric expansion. In P2 and P3, thicker soils were formed from the weathering of deep mobile regolith and were affected by near surface mobile regolith and surface mixing. Slopes and distances are purely illustrative but height variations were represented in accordance with modeling results.

Figure 9: corrected denudation rates calculated from equation 4 by assuming a uniform cosmic ray exposure time across the watershed equal to the exposure time determined on depth profiles (t=19 kyr). Corrected denudation rates written in black are inferred from ^{10}Be concentrations measured in topsoil, rock outcrop and stream sediment samples. We used in calculations the density of 2.7 g.cm^{-3} for rock outcrops and the average regolith density of 1.7 g.cm^{-3} for topsoil and stream sediment samples. Denudation rate written in blue is determined through the modeling of high resolution depth profiles without assumption of steady state ^{10}Be concentrations (d, equation 4). Denudation rate written in bold black for the outlet subcatchment is calculated from equation 10. Denudation rates are expressed in mm.kyr^{-1} and uncertainties include the uncertainties on the ^{10}Be concentrations, blank correction, and ^{10}Be production rates (uncertainties in table 2).

Table caption

Table 1: sample type, depth, bulk density, integrated density and ^{10}Be data for the three high resolution depth profiles from the southern part of the Strengbach watershed.

Table 2: sample type, location, elevation and ^{10}Be data for topsoil, rock outcrop and stream sediment samples collected across the Strengbach watershed. Maximum denudation rates (d_{max}) were inferred from the GIS toolbox Basinga (Charreau et al., 2019) using equation 9 and assuming a steady state of ^{10}Be concentrations. A constant bedrock density of 2.7 g.cm^{-3} was used in d_{max} calculations. Corrected denudation rates d were calculated without assuming a steady state of ^{10}Be

concentrations (equation 4) by using inherited ^{10}Be and cosmic ray exposure age determined on depth profiles. The density of 2.7 g.cm^{-3} for rock outcrops and the average regolith density of 1.7 g.cm^{-3} for topsoil and stream sediment samples were used in corrected d calculations.

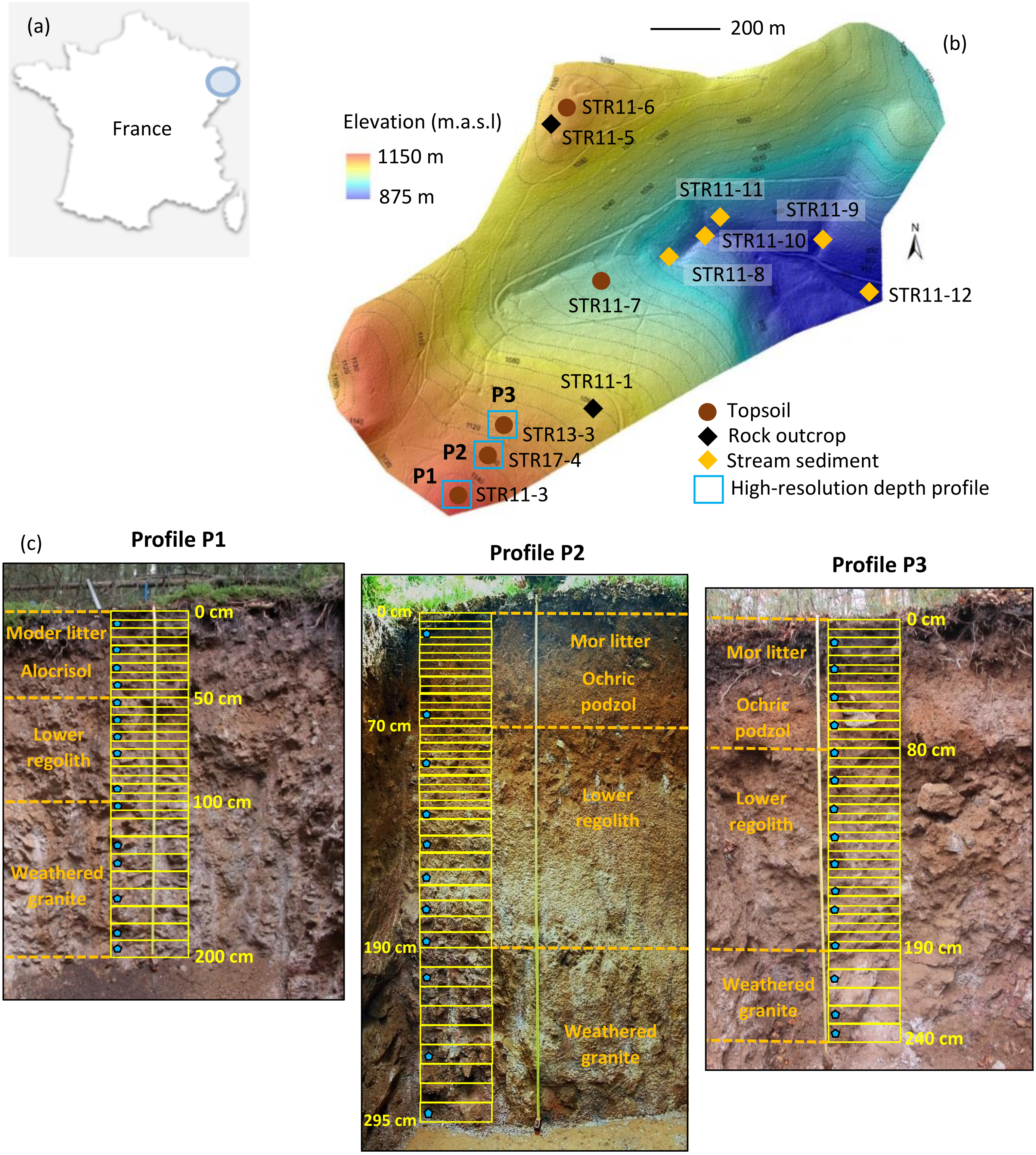
(a)
France
Elevation (m.a.s.l)
1150 m
875 m
200 m
(b)
STR11-6
STR11-5
STR11-11
STR11-9
STR11-10
STR11-8
STR11-12
STR11-7
STR11-1
P3
STR13-3
P2
STR17-4
P1
STR11-3
N
Topsoil
Rock outcrop
Stream sediment
High-resolution depth profile
(c)
Profile P1
0 cm
Moder litter
Alocrisol
50 cm
Lower
regolith
100 cm
Weathered
granite
200 cm
Profile P2
0 cm
Mor litter
Ochric
podzol
70 cm
Lower
regolith
190 cm
Weathered
granite
295 cm
Profile P3
0 cm
Mor litter
Ochric
podzol
80 cm
Lower
regolith
190 cm
Weathered
granite
240 cm

Figure 1

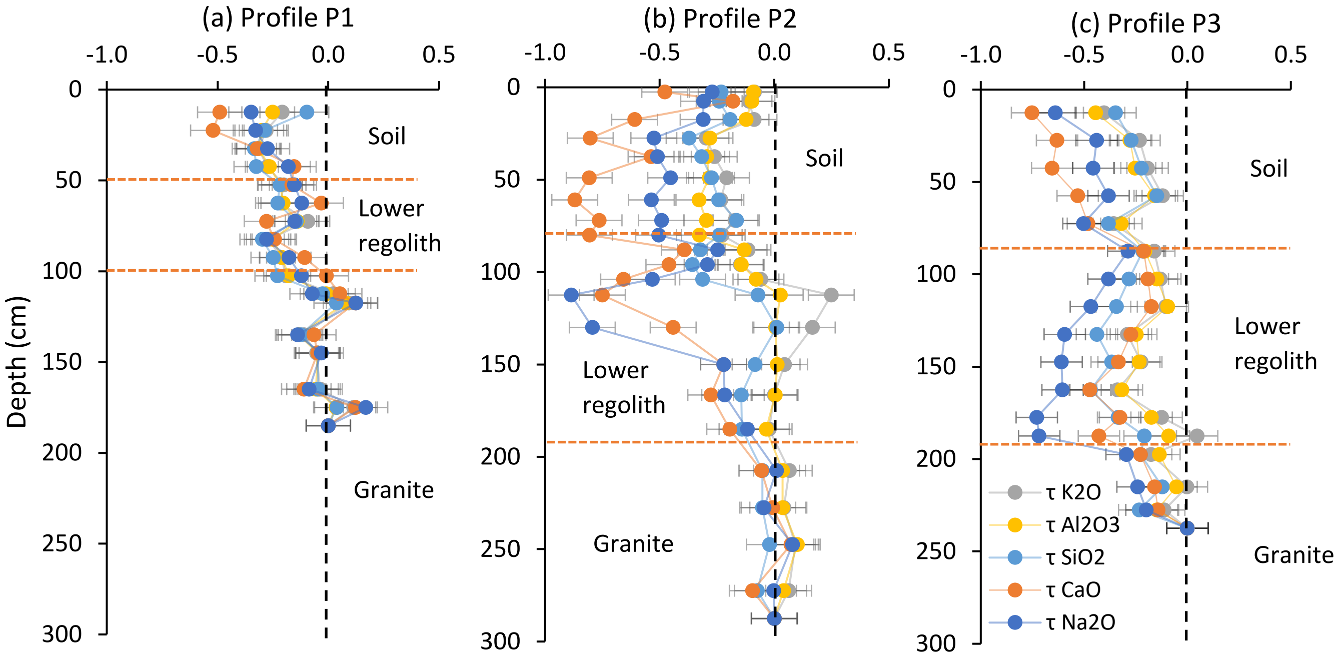
(a) Profile P1
(b) Profile P2
(c) Profile P3
-1.0
-0.5
0.0
0.5
0
50
100
150
200
250
300
Depth (cm)
Soil
Lower regolith
Granite
τ K2O
τ Al2O3
τ SiO2
τ CaO
τ Na2O

Figure 2

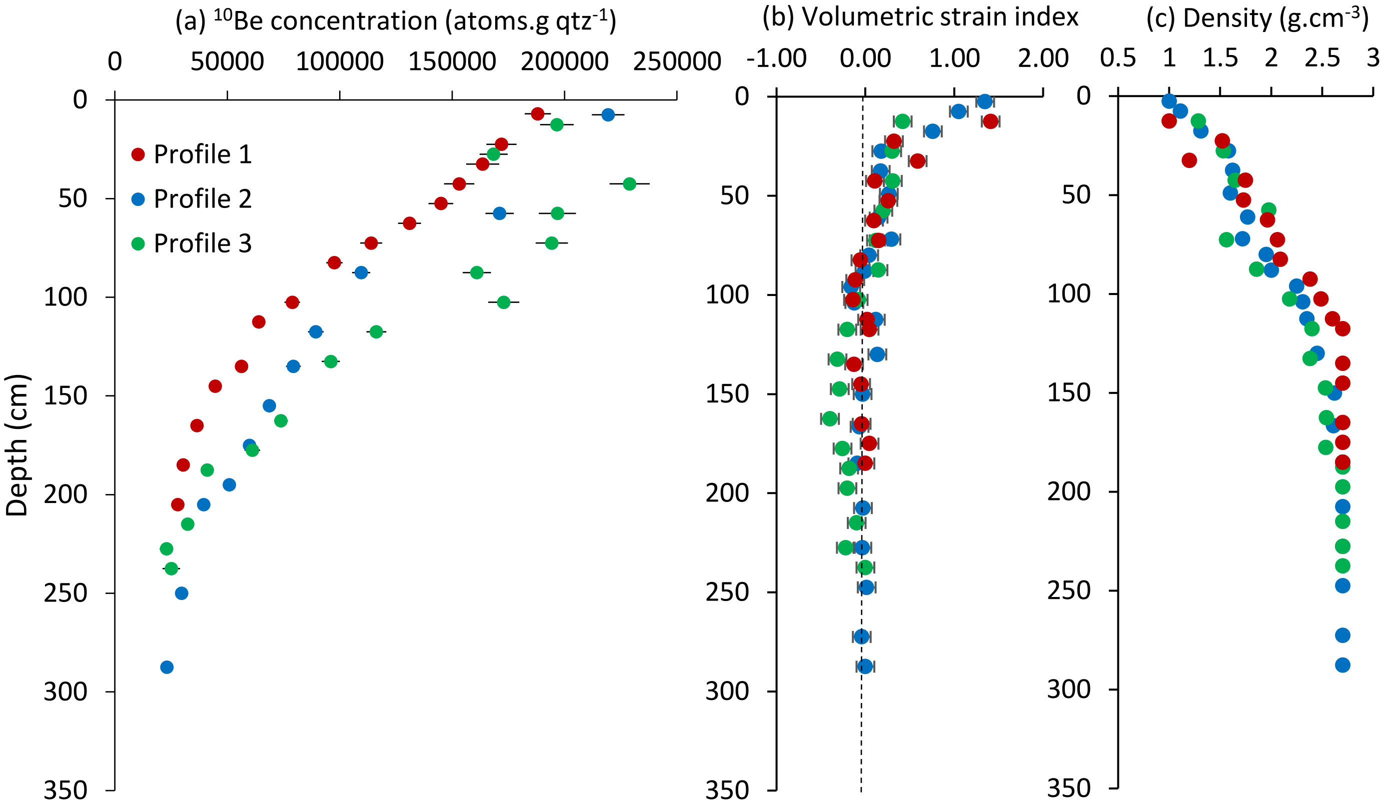
(a) ^{10}Be concentration (atoms.g qtz^{-1})
0
50000
100000
150000
200000
250000
Depth (cm)
0
50
100
150
200
250
300
350
● Profile 1
● Profile 2
● Profile 3
(b) Volumetric strain index
-1.00
0.00
1.00
2.00
(c) Density (g.cm^{-3})
0.5
1
1.5
2
2.5
3

Figure 3

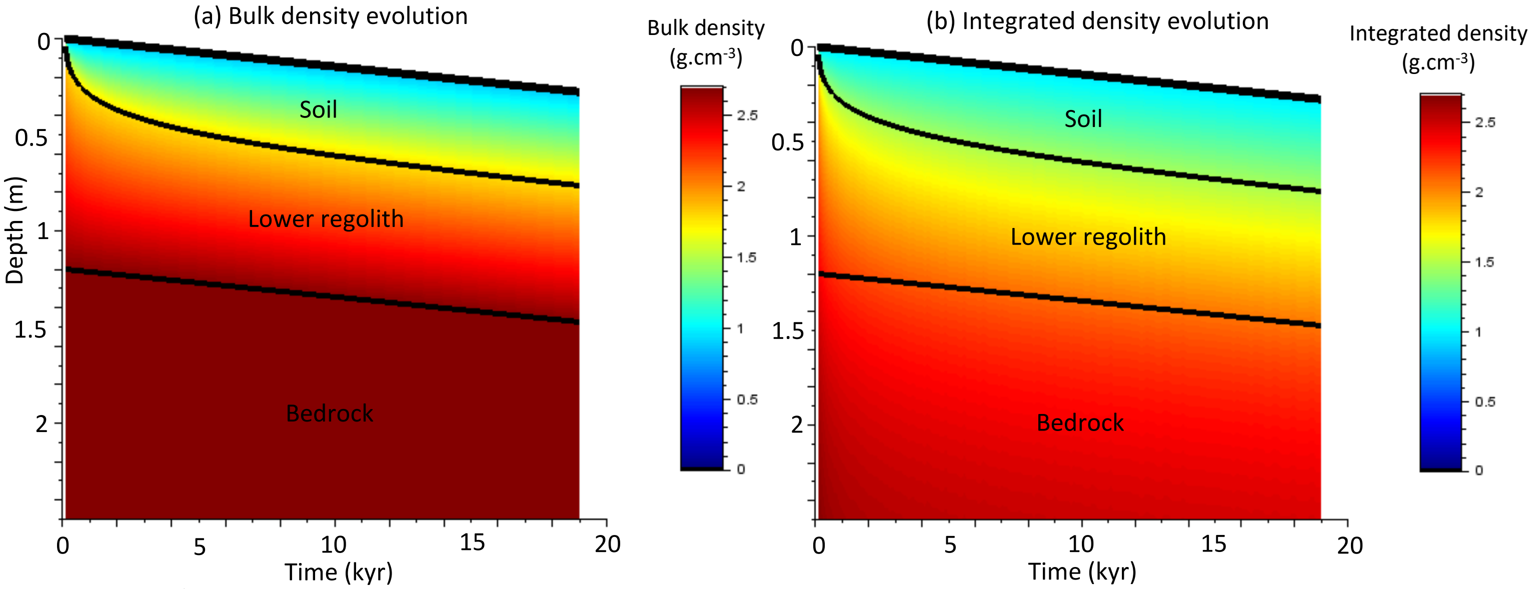

(a) Bulk density evolution

(b) Integrated density evolution

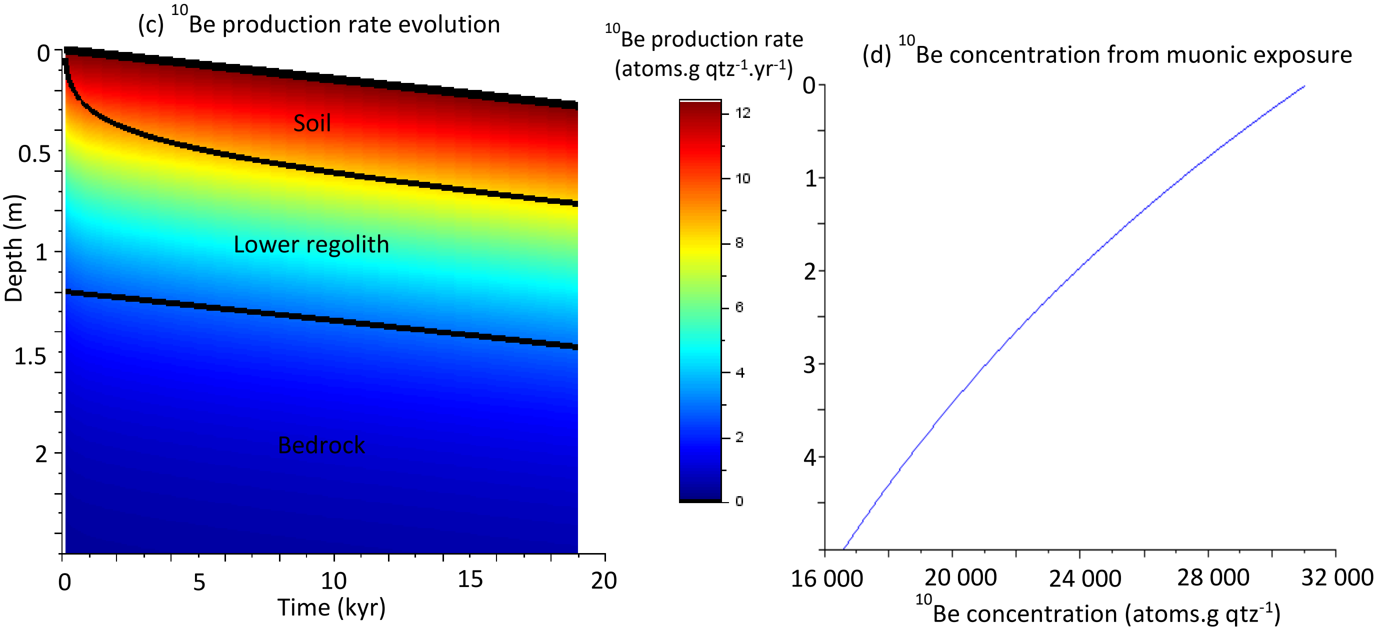

(c) ^{10}Be production rate evolution

(d) ^{10}Be concentration from muonic exposure

Figure 4

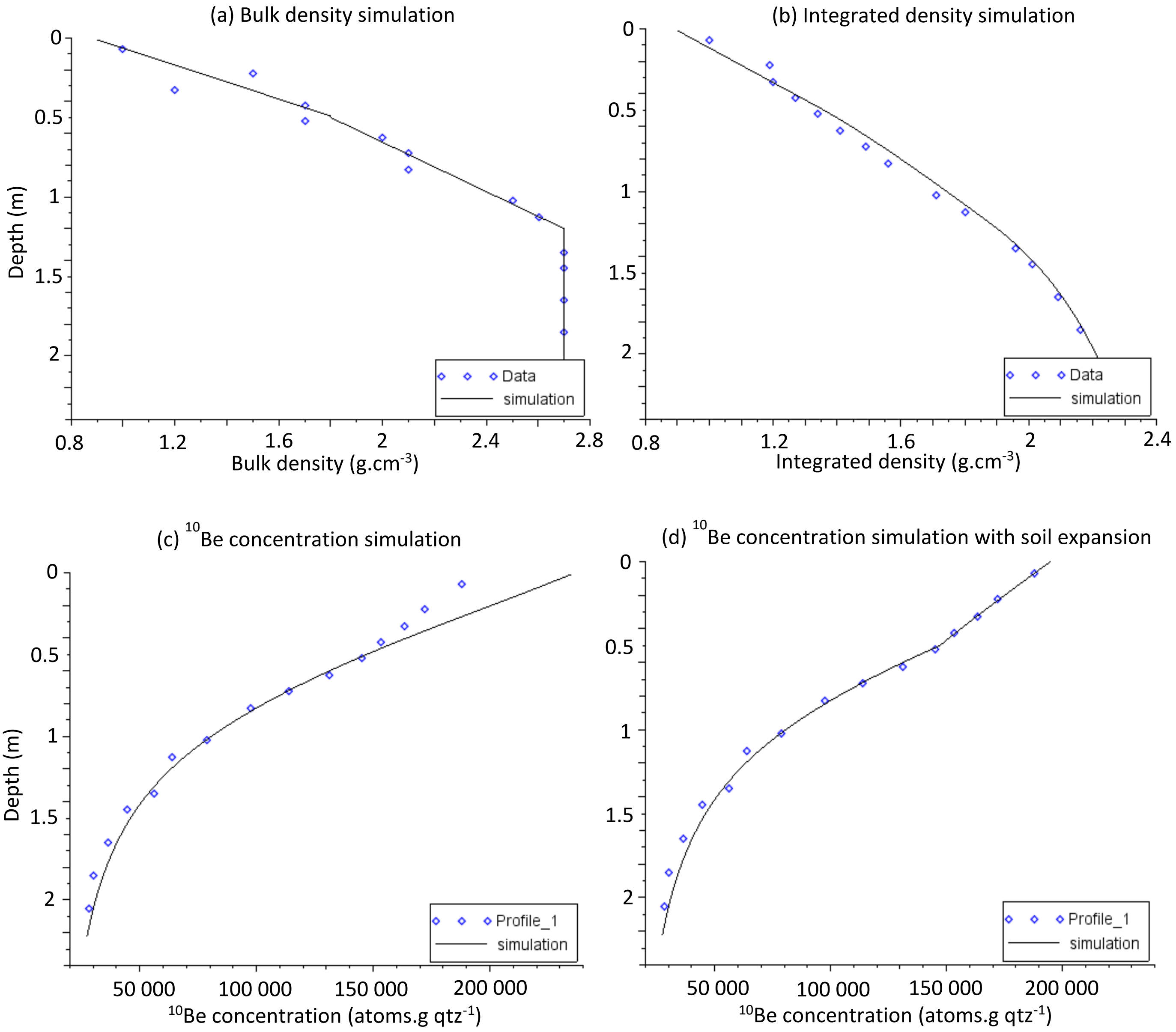
(a) Bulk density simulation
Depth (m)
0
0.5
1
1.5
2
0.8
1.2
1.6
2
2.4
2.8
Bulk density (g.cm-3)
Data
simulation
(b) Integrated density simulation
0
0.5
1
1.5
2
0.8
1.2
1.6
2
2.4
Integrated density (g.cm-3)
Data
simulation
(c) 10Be concentration simulation
Depth (m)
0
0.5
1
1.5
2
50 000
100 000
150 000
200 000
10Be concentration (atoms.g qtz-1)
Profile_1
simulation
(d) 10Be concentration simulation with soil expansion
0
0.5
1
1.5
2
50 000
100 000
150 000
200 000
10Be concentration (atoms.g qtz-1)
Profile_1
simulation

Figure 5

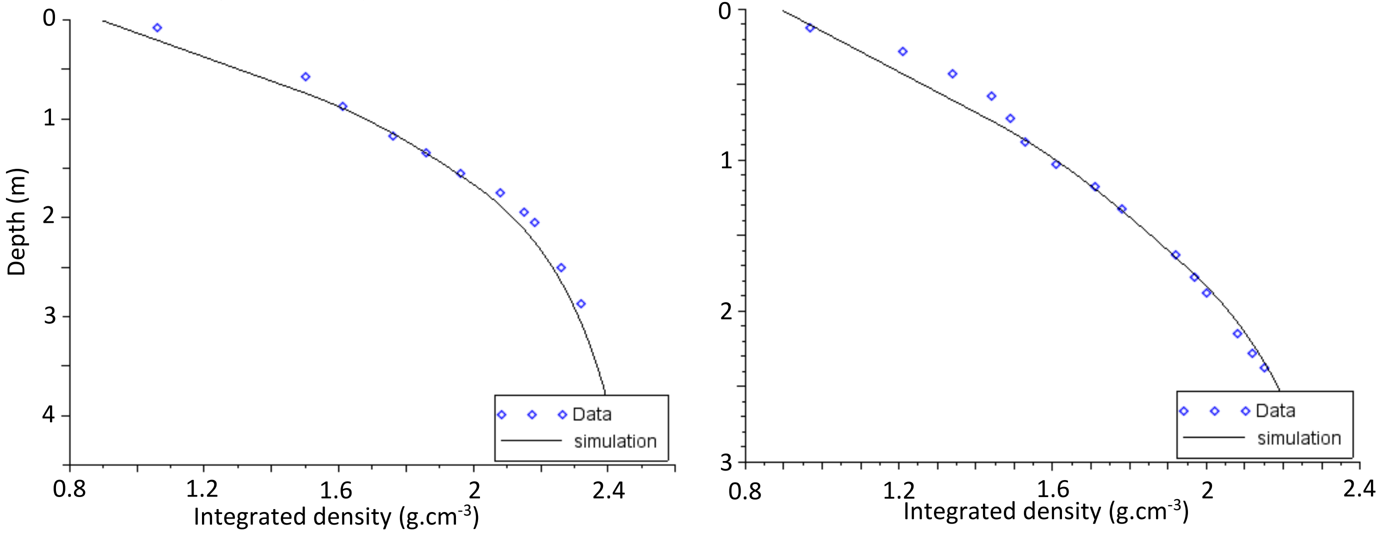
(a) Integrated density simulation (profile 2)

(b) Integrated density simulation (profile 3)

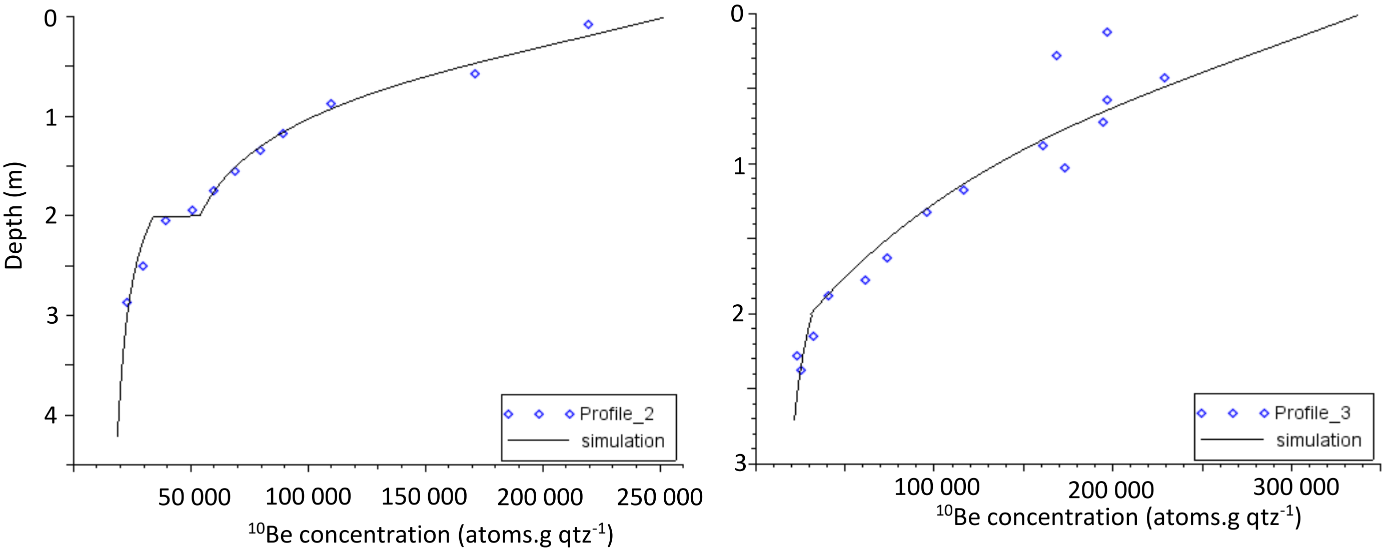
(c) ^{10}Be concentration simulation (profile 2)

(d) ^{10}Be concentration simulation (profile 3)

Figure 6

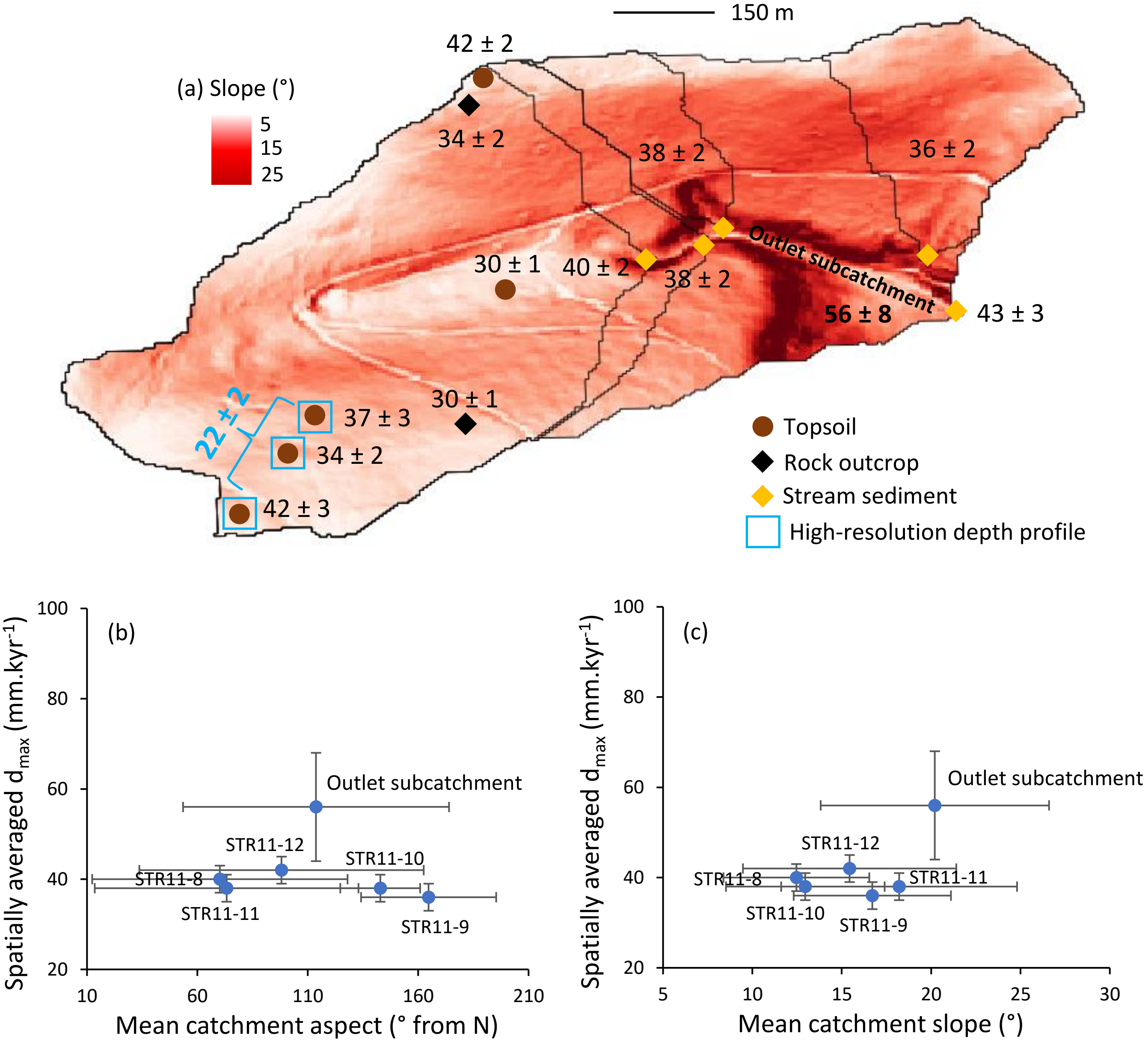
150 m
(a) Slope (°)
5
15
25
42 ± 2
34 ± 2
38 ± 2
36 ± 2
30 ± 1
40 ± 2
38 ± 2
Outlet subcatchment
56 ± 8
43 ± 3
30 ± 1
37 ± 3
34 ± 2
42 ± 3
22 ± 2
● Topsoil
◆ Rock outcrop
◆ Stream sediment
☐ High-resolution depth profile
(b)
Spatially averaged d_{max} (mm.kyr^{-1})
100
80
60
40
20
10
60
110
160
210
Mean catchment aspect (° from N)
Outlet subcatchment
STR11-12
STR11-10
STR11-8
STR11-11
STR11-9
(c)
Spatially averaged d_{max} (mm.kyr^{-1})
100
80
60
40
20
5
10
15
20
25
30
Mean catchment slope (°)
Outlet subcatchment
STR11-12
STR11-8
STR11-11
STR11-10
STR11-9

Figure 7

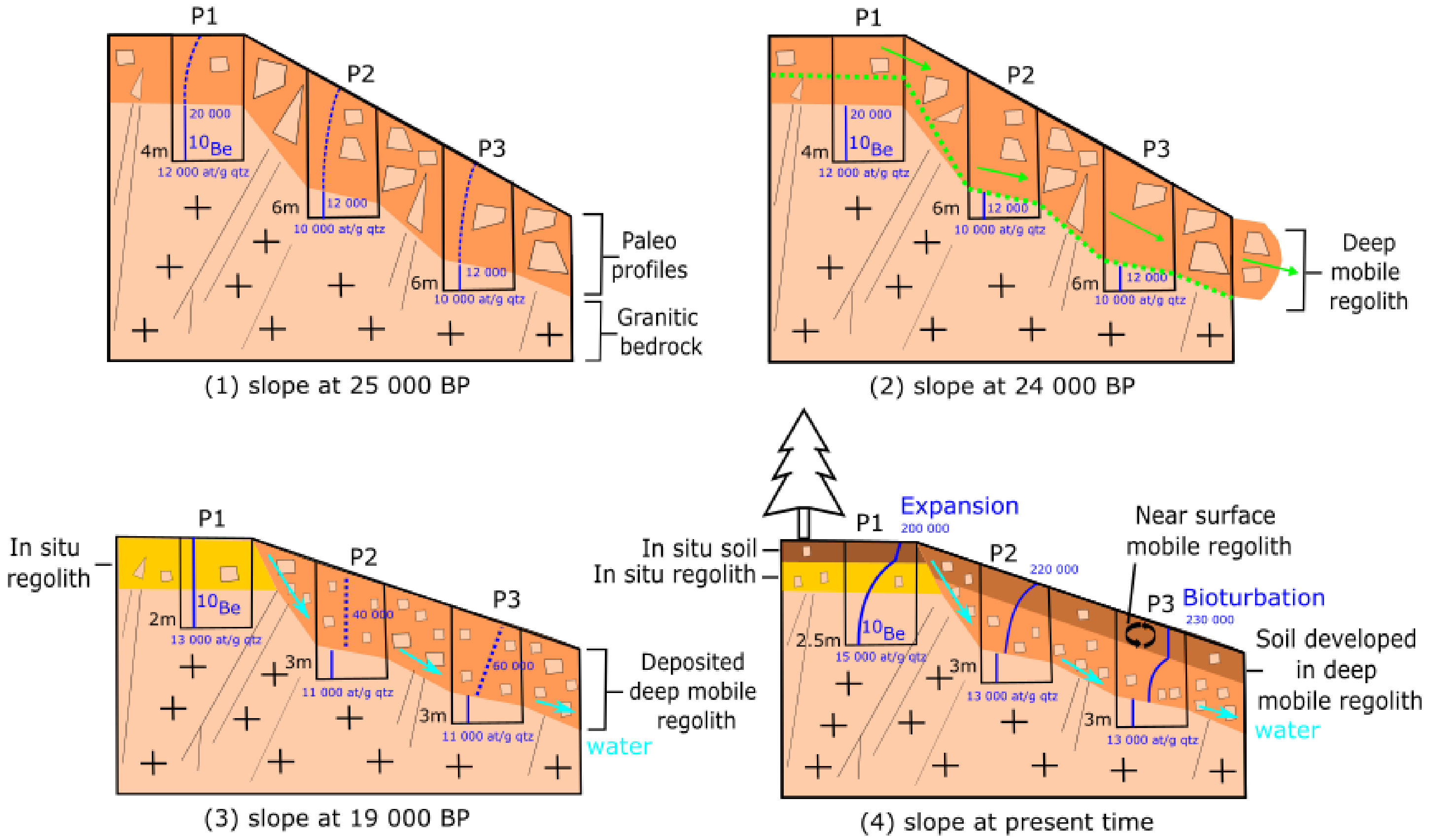

(1) slope at 25 000 BP

(2) slope at 24 000 BP

(3) slope at 19 000 BP

(4) slope at present time

Figure 8

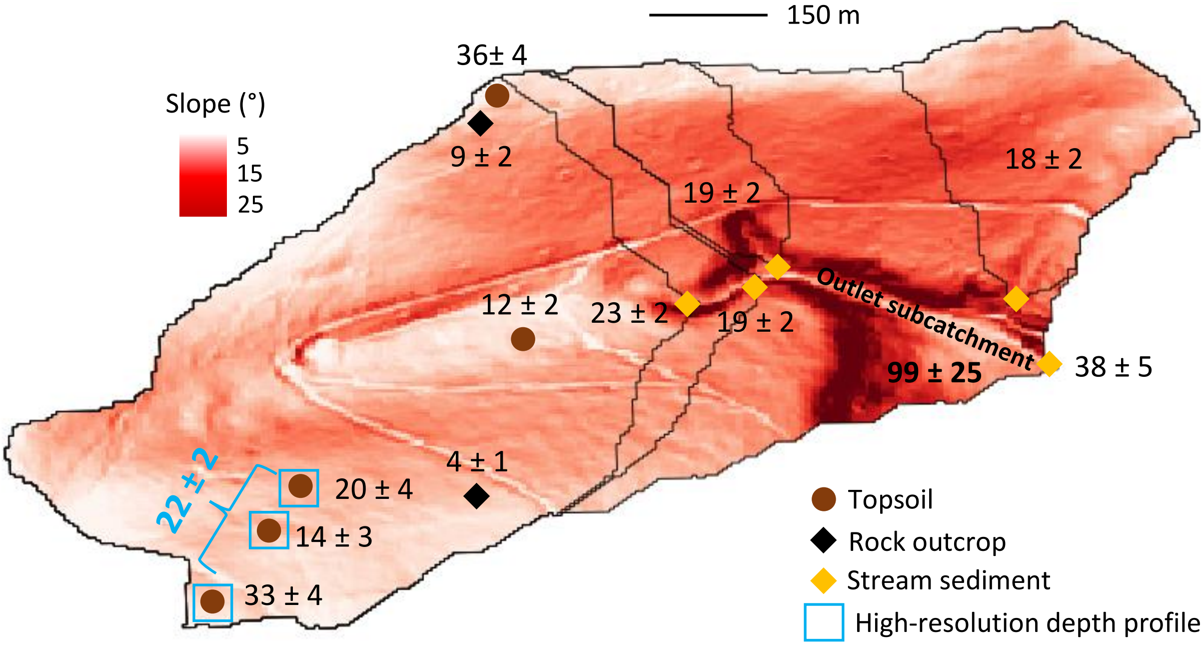
150 m
Slope (°)
5
15
25
36± 4
9 ± 2
19 ± 2
18 ± 2
12 ± 2
23 ± 2
19 ± 2
Outlet subcatchment
99 ± 25
38 ± 5
22 ± 2
20 ± 4
14 ± 3
33 ± 4
4 ± 1
Topsoil
Rock outcrop
Stream sediment
High-resolution depth profile

Figure 9

Sample	Type	Depth (cm)	Bulk density (g.cm^{-3})	Integrated density (g.cm^{-3})	Quartz mass (g)	^{9}Be (mg)	^{10}Be/^{9}Be	Err (%)	In-situ ^{10}Be (atoms. g qtz^{-1})	Err (%)
Profile P1 (48.208 °N, 7.191 °E, 1146 m)										
STR11-3	Soil	7.0	1.0	0.9	25.02	0.477	1.47E-13	3.1	188144	3.5
STR13-43	Soil	22.5	1.5	1.2	17.23	0.285	1.55E-13	3.4	171954	3.9
STR13-45	Soil	32.5	1.2	1.2	19.72	0.293	1.65E-13	4.0	163601	4.5
STR13-47	Soil	42.5	1.7	1.3	14.68	0.290	1.16E-13	3.9	153162	4.4
STR13-49	Soil	52.5	1.7	1.3	22.54	0.287	1.70E-13	3.9	144995	4.4
STR13-51	Lower regolith	62.5	2.0	1.4	18.60	0.277	1.32E-13	3.3	131079	3.9
STR13-53	Lower regolith	72.5	2.1	1.5	23.79	0.281	1.45E-13	3.8	114030	4.3
STR13-55	Lower regolith	82.5	2.1	1.6	22.03	0.252	1.23E-13	3.2	97672	3.7
STR13-59	Lower regolith	102.5	2.5	1.7	22.45	0.303	8.75E-14	3.9	78918	4.4
STR13-61	Bedrock	112.5	2.6	1.8	18.32	0.274	6.39E-14	4.0	63992	4.5
STR13-42B	Bedrock	135.0	2.7	1.9	29.31	0.291	8.49E-14	3.9	56360	4.4
STR13-43B	Bedrock	145.0	2.7	2.0	40.35	0.248	1.09E-13	5.2	44712	5.5
STR13-45B	Bedrock	165.0	2.7	2.1	38.00	0.278	7.48E-14	4.5	36532	4.9
STR13-47B	Bedrock	185.0	2.7	2.2	48.84	0.268	8.31E-14	3.9	30440	4.4
STR13-49B	Bedrock	205.0	2.7	2.2	57.09	0.280	8.55E-14	3.8	28057	4.3
Profile P2 (48.20900 °N, 7.19214 °E, 1131 m)										
STR17-4	Soil	7.5	1.1	1.1	25.49	0.519	1.61E-13	2.6	219429	3.3
STR17-14	Soil	57.5	1.9	1.5	21.67	0.518	1.08E-13	3.1	171153	3.7
STR17-20	Lower regolith	87.5	2.3	1.6	24.30	0.514	7.79E-14	3.1	109549	3.7
STR17-26	Lower regolith	117.5	2.6	1.8	30.84	0.511	8.01E-14	3.3	89399	3.9
STR17-28	Lower regolith	135.0	2.7	1.9	32.12	0.515	7.38E-14	3.6	79421	4.1
STR17-30	Lower regolith	155.0	2.7	2.0	37.16	0.516	7.41E-14	3.1	68662	3.7
STR17-32	Lower regolith	175.0	2.7	2.1	34.09	0.515	5.87E-14	3.1	59877	3.7
STR17-34	Bedrock	195.0	2.7	2.2	31.20	0.521	4.58E-14	3.4	50977	3.9
STR17-36	Bedrock	205.0	2.7	2.2	31.14	0.519	3.55E-14	4.0	39510	4.4
STR17-40	Bedrock	250.0	2.7	2.3	38.61	0.519	3.31E-14	4.9	29688	5.3
STR17-43	Bedrock	287.5	2.7	2.3	36.58	0.518	2.45E-14	6.1	23124	6.4
Profile P3 (48.209 °N, 7.193 °E, 1120 m)										
STR13-3	Soil	12.5	1.3	1.0	21.0	0.295	2.17E-13	3.2	196609	3.8
STR13-6	Soil	27.5	1.5	1.2	15.6	0.298	1.30E-13	3.1	168477	3.7
STR13-9	Soil	42.5	1.6	1.3	13.5	0.294	1.56E-13	3.3	228979	3.9
STR13-12	Soil	57.5	1.9	1.4	18.7	0.295	1.88E-13	3.7	196839	4.2
STR13-15	Soil	72.5	1.6	1.5	16.0	0.297	1.53E-13	3.1	194345	3.7
STR13-18	Lower regolith	87.5	1.9	1.6	17.6	0.297	1.39E-13	3.3	161022	3.9
STR13-21	Lower regolith	102.5	2.2	1.7	24.4	0.295	2.18E-13	3.4	172978	4.0
STR13-24	Lower regolith	117.5	2.4	1.7	14.3	0.294	8.81E-14	3.2	116320	3.8
STR13-27	Lower regolith	132.5	2.4	1.8	13.8	0.295	6.94E-14	3.7	96054	4.2
STR13-33	Lower regolith	162.5	2.5	1.9	21.6	0.297	8.00E-14	3.6	73919	4.1
STR13-36	Lower regolith	177.5	2.5	2.0	32.4	0.312	9.57E-14	5.3	61181	5.6
STR13-26B	Bedrock	187.5	2.7	2.0	47.4	0.314	9.50E-14	6.9	41096	7.2
STR13-28B	Bedrock	215.0	2.7	2.1	48.8	0.313	9.06E-14	7.1	32472	7.4
STR13-29B	Bedrock	227.5	2.7	2.1	30.1	0.295	3.74E-14	13	22949	13
STR13-30B	Bedrock	237.5	2.7	2.1	58.3	0.311	9.99E-14	15	25116	15

Sample	**Type**	**Location**	**Elevation (m)**	**Quartz mass (g)**	**^{9}Be (mg)**	**^{10}Be/^{9}Be**	**Err (%)**	**In-situ ^{10}Be (atoms. g qtz^{-1})**	**Err (%)**	**d$_{max}$ (mm.kyr^{-1})**	**Corrected d (mm.kyr^{-1})**
STR11-1	Rock outcrop	48.20951 °N - 7.19587 °E	1115	25.09	0.469	1.87E-13	3.5	233458	4.0	30±1	4±1
STR11-5	Rock outcrop	48.21582 °N - 7.19528 °E	1117	24.96	0.487	1.68E-13	3.2	218546	3.7	34±2	9±2
STR11-3	Soil (top profile P1)	48.20817 °N - 7.19111 °E	1146	25.02	0.477	1.45E-13	3.1	185587	3.7	42±3	33±4
STR17-4	Soil (top profile P2)	48.20900 °N - 7.19214 °E	1131	25.49	0.518	4.82E-13	2.6	219429	3.3	34±2	14±3
STR13-3	Soil (top profile P3)	48.20942 °N - 7.19278 °E	1120	20.97	0.295	2.17E-13	3.2	204375	3.8	37±3	20±4
STR11-6	Soil	48.21621 °N - 7.19550 °E	1110	39.95	0.473	2.28E-13	3.1	180207	3.6	42±2	36±4
STR11-7	Soil	48.21300 °N - 7.19646 °E	1017	29.96	0.474	2.13E-13	3.3	225541	3.9	30±1	12±2
STR11-8	Stream sediments	48.21319 °N - 7.19866 °E	986	39.91	0.501	2.18E-13	3.1	182825	3.7	40±2	23±2
STR11-9	Stream sediments	48.21341 °N - 7.20348 °E	922	40.86	0.508	2.28E-13	3.0	189279	3.6	36±2	18±2
STR11-10	Stream sediments	48.21357 °N - 7.19994 °E	962	39.34	0.500	2.22E-13	3.1	188241	3.7	38±2	19±2
STR11-11	Stream sediments	48.21377 °N - 7.20012 °E	964	40.06	0.481	2.34E-13	3.0	188057	3.6	38±2	19±2
STR11-12	Stream sediments	48.21214 °N- 7.20447 °E	891	39.35	0.504	1.87E-13	3.1	159699	3.7	43±3	38±5

Supplementary materials

Supplementary tables

Sample	Type	Depth (cm)	Quartz (%)	Plagioclase Feldspars (%)	K-feldspars (%)	Micas and illites (%)	Kaolinite (%)	Interstratified clays (%)	Hematite (%)
Profile P1 (48.208 °N, 7.191 °E, 1146 m)									
STR13-41	Soil	12.5	43	17	25	8	2	5	0
STR13-43	Soil	22.5	43	18	25	8	1	5	0
STR13-45	Soil	32.5	40	20	23	9	2	6	0
STR13-47	Soil	42.5	37	22	26	8	2	5	0
STR13-49	Soil	52.5	38	18	31	9	3	1	0
STR13-51	Lower regolith	62.5	46	15	21	16	2	0	0
STR13-53	Lower regolith	72.5	48	15	18	17	2	0	0
STR13-55	Lower regolith	82.5	52	16	17	11	4	0	0
STR13-57	Lower regolith	92.5	45	16	22	15	2	0	0
STR13-59	Bedrock	102.5	35	22	22	20	1	0	0
STR13-61	Bedrock	112.5	34	20	26	19	0	0	1
STR13-41B	Bedrock	117.5	37	18	29	14	2	0	0
STR13-42B	Bedrock	135	40	22	22	13	2	0	1
STR13-43B	Bedrock	145	33	19	30	14	2	0	2
STR13-45B	Bedrock	165	37	22	28	11	2	0	0
STR13-47B	Bedrock	185	32	20	29	17	2	0	0
Profile P2 (48.20900 °N, 7.19214 °E, 1131 m)									
STR17-4	Soil	7.5	51	11	20	7	1	10	0
STR17-6	Soil	17.5	49	10	20	12	1	7	0
STR-17-8	Soil	27.5	48	13	23	7	1	8	0
STR17-12	Soil	49	48	14	22	6	1	9	0
STR17-14	Soil	61	47	16	25	10	1	0	0
STR17-18	Lower regolith	80	38	15	20	27	0	0	0
STR17-20	Lower regolith	88	38	18	20	24	0	0	0
STR17-24	Lower regolith	104	40	10	20	24	1	4	1
STR17-26	Lower regolith	112.5	51	4	21	16	0	6	1
STR17-28	Lower regolith	130	55	4	15	24	0	1	1
STR17-30	Lower regolith	150	43	15	18	24	0	0	0
STR17-32	Lower regolith	166.5	45	17	18	15	0	4	1
STR17-36	Bedrock	207.5	43	17	20	19	0	1	0
STR17-40	Bedrock	247.5	43	18	17	21	0	1	0
STR17-43	Bedrock	287.5	48	17	16	18	0	1	0
Profile P3 (48.209 °N, 7.193 °E, 1120 m)									
STR13-3	Soil	12.5	46	15	25	8	3	3	0
STR13-6	Soil	27.5	39	19	26	9	1	6	0
STR13-9	Soil	42.5	42	17	27	8	1	5	0
STR13-12	Soil	57.5	43	19	25	7	2	4	0
STR13-15	Soil	72.5	41	20	26	8	4	1	0
STR13-18	Lower regolith	87.5	38	21	26	14	1	0	1
STR13-21	Lower regolith	102.5	42	23	23	10	3	0	1
STR13-24	Lower regolith	117.5	33	18	18	29	0	0	1
STR13-27	Lower regolith	132.5	30	19	20	31	0	0	0
STR13-30	Lower regolith	147.5	35	16	21	28	0	0	0
STR13-33	Lower regolith	162.5	33	18	20	26	3	0	1
STR13-36	Lower regolith	177.5	44	6	24	24	0	2	0
STR13-26B	Bedrock	187.5	40	10	24	26	0	0	1
STR13-27B	Bedrock	197.5	37	23	24	13	3	0	0
STR13-28B	Bedrock	215	39	20	24	17	0	0	0
STR13-29B	Bedrock	227.5	36	25	24	15	0	0	1
STR13-30B	Bedrock	237.5	35	26	24	15	0	0	0

Table S1: mineralogical composition of the samples collected within the three depth profiles from the southern part of the Strengbach watershed. The mineralogical compositions of all the powdered 250-µm bulk samples were determined by XRD with a Siemens D5000 diffractometer (BRGM) or a X BRUKER

D8 ADVANCE Eco Diffractometer (ITES). The <2 µm clay fractions were separated by centrifugation and analyzed after air drying and treatment with glycol ethylene and hydrazine to distinguish illites, smectites, kaolinites and inter-stratified clay minerals. Estimation of mineral proportion has been performed by the Rietveld method with the Siroquant software. (Uncertainty of ≈ 3 % for quartz and plagioclase mass proportion and ≈5 % for micas and clay minerals.

Sample	Type	Depth (cm)	SiO_2 (%)	Al_2O_3 (%)	CaO (%)	Na_2O (%)	K_2O (%)	MgO (%)	TiO_2 (%)
Profile P1 (48.208 °N, 7.191 °E, 1146 m)									
STR13-41	Soil	12.5	73.2	12.0	0.16	1.7	4.5	0.21	0.18
STR13-43	Soil	22.5	69.3	13.5	0.18	2.1	4.9	0.26	0.21
STR13-45	Soil	32.5	68.5	14.0	0.27	2.4	5.0	0.32	0.22
STR13-47	Soil	42.5	68.1	14.7	0.33	2.6	5.2	0.36	0.22
STR13-49	Soil	52.5	70.2	13.9	0.29	2.4	5.1	0.30	0.20
STR13-51	Lower regolith	62.5	70.1	14.4	0.34	2.6	5.1	0.34	0.20
STR13-53	Lower regolith	72.5	70.6	14.1	0.23	2.2	5.3	0.26	0.18
STR13-55	Lower regolith	82.5	69.5	14.8	0.29	2.3	5.1	0.39	0.22
STR13-57	Lower regolith	92.5	69.6	14.6	0.32	2.4	5.2	0.39	0.20
STR13-59	Bedrock	102.5	70.2	14.9	0.35	2.6	5.2	0.20	0.20
STR13-61	Bedrock	112.5	71.8	14.5	0.30	2.2	5.3	0.20	0.16
STR13-41B	Bedrock	117.5	71.6	14.8	0.30	2.5	5.3	0.20	0.15
STR13-42B	Bedrock	135	72.6	14.3	0.30	2.3	5.2	0.25	0.18
STR13-43B	Bedrock	145	72.6	14.4	0.28	2.4	5.1	0.26	0.17
STR13-45B	Bedrock	165	72.1	14.2	0.26	2.2	5.2	0.20	0.16
STR13-46B	Bedrock	175	71.8	14.2	0.30	2.6	5.5	0.26	0.15
STR13-47B	Bedrock	185	72.4	14.4	0.28	2.3	5.1	0.39	0.16
Profile P2 (48.20900 °N, 7.19214 °E, 1131 m)									
STR17-3	Soil	2.5	67.7	13.7	0.21	1.7	4.9	0.30	0.16
STR17-4	Soil	7.5	69.0	14.0	0.34	1.7	4.9	0.32	0.16
STR17-6	Soil	17.5	72.4	13.4	0.16	1.7	4.9	0.26	0.16
STR-17-8	Soil	27.5	69.8	13.6	0.10	1.4	4.7	0.29	0.20
STR17-10	Soil	37.5	74.4	13.1	0.23	1.4	4.9	0.27	0.20
STR17-12	Soil	49	74.3	12.5	0.09	1.5	4.9	0.24	0.19
STR17-14	Soil	61	77.0	11.7	0.06	1.2	4.7	0.22	0.19
STR17-16	Lower regolith	72	77.6	11.2	0.10	1.2	4.7	0.21	0.17
STR17-18	Lower regolith	80	77.3	11.7	0.09	1.4	4.8	0.23	0.19
STR17-20	Lower regolith	88	70.8	15.5	0.29	2.1	5.6	0.36	0.19
STR17-22	Lower regolith	96	70.2	16.0	0.27	2.1	5.7	0.40	0.20
STR17-24	Lower regolith	104	70.3	16.1	0.16	1.3	5.9	0.47	0.19
STR17-26	Lower regolith	112.5	73.2	13.8	0.09	0.2	6.0	0.50	0.14
STR17-28	Lower regolith	130	75.2	12.8	0.19	0.4	5.3	0.47	0.14
STR17-30	Lower regolith	150	74.7	14.1	0.29	1.7	5.2	0.35	0.15
STR17-32	Lower regolith	166.5	72.6	14.5	0.28	1.8	5.2	0.37	0.15
STR17-34	Bedrock	185	72.4	13.9	0.31	2.0	5.0	0.32	0.15
STR17-36	Bedrock	207.5	74.7	13.9	0.34	2.1	5.1	0.29	0.14
STR17-38	Bedrock	227.5	75.2	14.0	0.36	2.0	5.0	0.31	0.14
STR17-40	Bedrock	247.5	73.9	14.2	0.37	2.2	5.0	0.29	0.14
STR17-42	Bedrock	272.5	74.0	14.2	0.33	2.1	5.2	0.27	0.15
STR17-43	Bedrock	287.5	76.6	13.1	0.35	2.0	4.7	0.26	0.14
Profile P3 (48.209 °N, 7.193 °E, 1120 m)									
STR13-3	Soil	12.5	71.6	11.5	0.11	1.5	4.5	0.22	0.20
STR13-6	Soil	27.5	73.3	13.7	0.15	2.2	5.3	0.27	0.19
STR13-9	Soil	42.5	72.4	13.1	0.13	1.9	5.2	0.19	0.17
STR13-12	Soil	57.5	72.1	13.4	0.16	2.0	5.1	0.21	0.16
STR13-15	Soil	72.5	70.9	14.7	0.24	2.2	5.1	0.29	0.21
STR13-18	Lower regolith	87.5	73.8	14.1	0.30	2.6	5.4	0.26	0.18
STR13-21	Lower regolith	102.5	71.4	16.0	0.33	2.3	6.0	0.35	0.19
STR13-24	Lower regolith	117.5	69.0	17.9	0.35	2.1	6.5	0.43	0.20
STR13-27	Lower regolith	132.5	69.0	17.4	0.36	1.9	6.0	0.45	0.23
STR13-30	Lower regolith	147.5	70.6	16.1	0.30	1.7	6.0	0.42	0.21
STR13-33	Lower regolith	162.5	69.9	16.9	0.28	2.0	6.0	0.47	0.24
STR13-36	Lower regolith	177.5	70.8	16.6	0.29	1.1	6.4	0.46	0.20
STR13-26B	Bedrock	187.5	72.1	15.6	0.21	1.0	6.6	0.43	0.17
STR13-27B	Bedrock	197.5	72.0	15.2	0.29	2.5	5.3	0.34	0.17
STR13-28B	Bedrock	215	72.4	14.7	0.28	2.4	5.7	0.29	0.15
STR13-29B	Bedrock	227.5	73.0	15.3	0.33	2.9	5.8	0.29	0.18
STR13-30B	Bedrock	237.5	74.3	14.0	0.30	2.8	5.1	0.26	0.14

Table S2: sample type, sampling depth and major element concentrations measured in the three high resolution depth profiles from the southern part of the Strengbach watershed (see Gangloff et al., 2014 or Prunier et al., 2015 for a detail of the analytical procedure).

	Profile P1	**Profile P2**	**Profile P3**
General parameters			
Profile depth (cm)	250	450	300
Space step (cm)	1	1	1
Time step (yr)	100	100	100
Total simulation time (yr)	19 000	19 000	19 000
Initial thicknesses			
Initial soil thickness (cm)	4	4	4
Initial regolith thickness (cm)	120	190	200
Soil and regolith evolution			
Mean denudation rate (d, cm.yr^{-1})	0.0022	0.0022	0.0022
Maximum regolith production rate (F_0, g.cm^{-2}.yr^{-1})	0.23	0.23	0.23
Scaling factor for soil (α,cm^{-1})	0.090	0.055	0.055
Scaling factor for regolith (β,cm^{-1})	0.034	0.034	0.034
Typical regolith production rate (mm.kyr^{-1})	14	3	2
Typical soil production rate (mm.kyr^{-1})	16	18	19
Density			
Average regolith density (g.cm^{-3})	1.7	1.7	1.7
Topsoil density (g.cm^{-3})	0.9	0.9	0.9
Soil base density (g.cm^{-3})	1.8	2.1	2.0
Bedrock density (g.cm^{-3})	2.7	2.7	2.7
In situ ^{10}Be			
C_0 in lower regolith (atoms g qtz^{-1})	Equals muonic pre-exposure (see figure 4d)	Constant value over depth of 40000 (full mixing of mobile regolith)	Variable value over depth between 15000 and 120000 (limited mixing of mobile regolith)
C_0 in bedrock (atoms g qtz^{-1})	Equals muonic pre-exposure (see figure 4d)	Equals muonic pre-exposure (see figure 4d)	Equals muonic pre-exposure (see figure 4d)
Attenuation length neutrons (K_n, g.cm^{-2})	150	150	150
Attenuation length fast muons (K_{fm}, g.cm^{-2}))	5300	5300	5300
Attenuation length negative muons (K_{nm}, g.cm^{-2})	1500	1500	1500
Surface total production rate (P, atoms g qtz^{-1}.yr^{-1})	12.43	12.24	12.05
Relative contribution neutrons (P_n)	0.9785	0.9785	0.9785
Relative contribution fast muons (P_{fm})	0.0065	0.0065	0.0065
Relative contribution negative muons (P_{nm})	0.0150	0.0150	0.0150

Table S3: variables and numerical values used for the direct modeling of the three depth profiles from the southern part of the watershed. P is the total production rate of ^{10}Be at the surface of the soil (determined with the Basinga GIS toolbox; Charreau et al., 2019). P_n, P_{nm} and P_{fm} are the relative contributions of 97.85, 1.5 and 0.65 % to the total production and K_n, K_{nm} and K_{fm} are the effective attenuation lengths of 150, 1500 and 5300 g.cm^{-2}, for secondary neutrons, negative muons and fast muons, respectively (Braucher et al., 2009). We used λ=5E-7 yr^{-1} for the radioactive decay constant of ^{10}Be.

Catchment	Outlet location	Outlet Elevation (m)	Area (m²)	Mean slope (°)	Mean orientation (° from N)	Spatially-averaged d_{max} (mm/kyr)	Corrected spatially-averaged d (mm/kyr)
STR11-8 catchment	48.21319 °N - 7.19866 °E	986	387370	12.5	70.2	40±2	23±2
STR11-9 catchment	48.21341 °N - 7.20348 °E	922	90856	16.7	164.7	36±2	18±2
STR11-10 catchment	48.21357 °N - 7.19994 °E	962	432397	12.9	73.2	38±2	19±2
STR11-11 catchment	48.21377 °N - 7.20012 °E	964	173057	18.2	142.8	38±2	19±2
STR11-12 catchment	48.21214 °N- 7.20447 °E	891	741344	15.4	98.1	43±3	38±5
Outlet subcatchment	48.21214 °N- 7.20447 °E	891	175011	20.2	113.7	56±8	99±25

Table S4: catchment characteristics for stream sediment samples collected across the Strengbach watershed. Maximum spatially-averaged denudation rates (spatially-averaged d_{max}) were inferred from the GIS toolbox Basinga (Charreau et al., 2019) using equation 9 and assuming a steady state of ^{10}Be concentrations. A constant bedrock density of 2.7 g.cm^{-3} was used in spatially-averaged d_{max} calculations. Corrected spatially-averaged denudation rates d were calculated without assuming a steady state of ^{10}Be concentrations (equation 4) by using inherited ^{10}Be and cosmic ray exposure age determined on depth profiles. The density of 1.7 g.cm^{-3} for stream sediment samples were used in corrected d calculations.

Supplementary figures

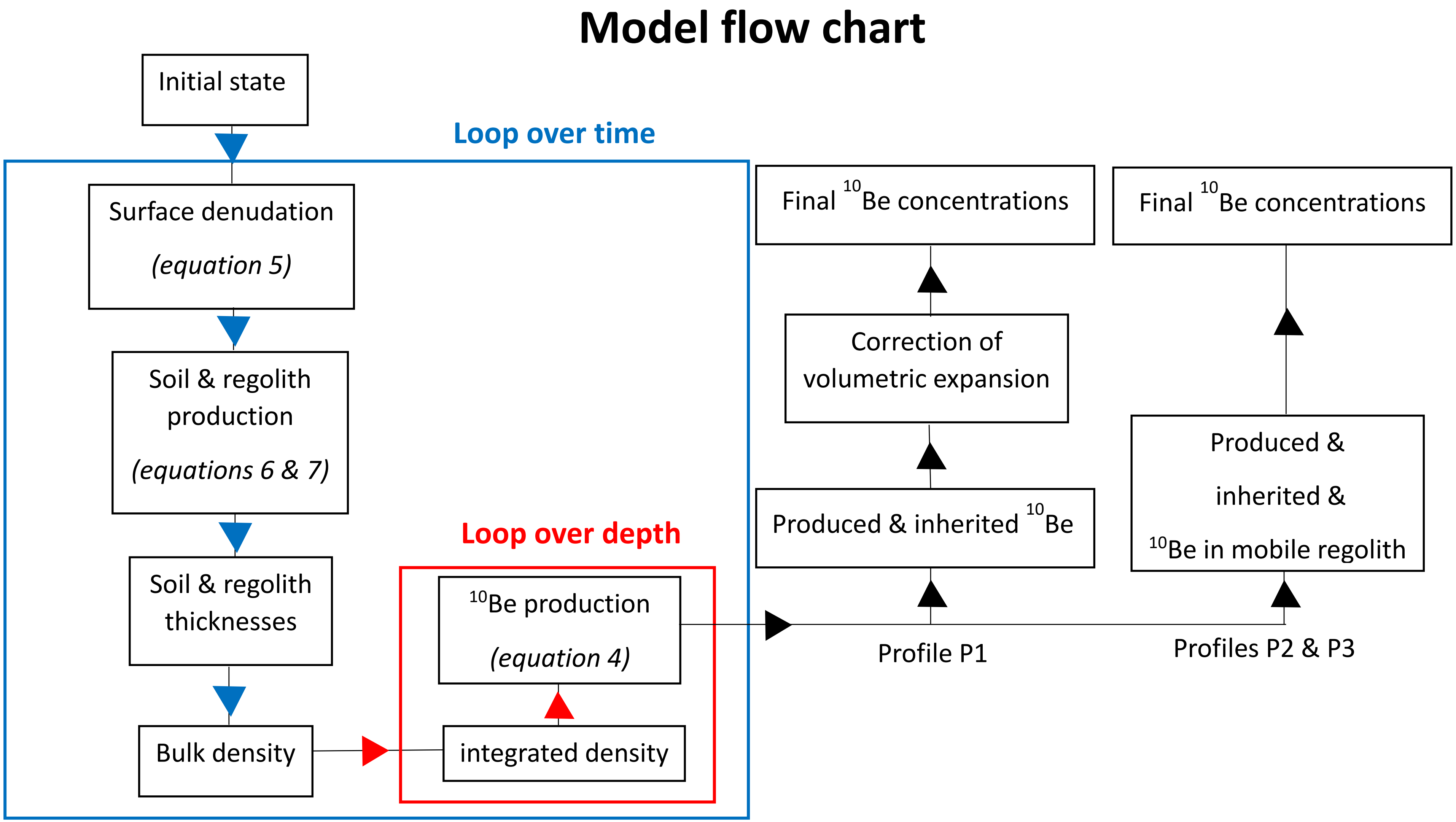

Figure S1: flow chart of the modeling of depth profile evolution and of ^{10}Be concentration.